Inorganic Chemistry

Article

pubs.acs.org/IC

Comparison of Amorphous Iridium Water-Oxidation Electrocatalysts Prepared from Soluble Precursors

James D. Blakemore,[†,∥] Nathan D. Schley,[†] Maxwell N. Kushner-Lenhoff,[†] Andrew M. Winter,[†] Francis D'Souza,*[,‡,§] Robert H. Crabtree,*[,†] and Gary W. Brudvig*[,†]

[†]Department of Chemistry, Yale University, P.O. Box 208107, New Haven, Connecticut 06520-8107, United States

[‡]Department of Chemistry, Wichita State University, Wichita, Kansas 67260-0051, United States

[§]Department of Chemistry, University of North Texas, Denton, Texas 76203, United States

Supporting Information

ABSTRACT: Electrodeposition of iridium oxide layers from soluble precursors provides a route to active thin-layer electrocatalysts for use on water-oxidizing anodes. Certain organometallic half-sandwich aqua complexes of iridium form stable and highly active oxide films upon electrochemical oxidation in aqueous solution. The catalyst films appear as blue layers on the anode when sufficiently thick, and most closely resemble hydrous iridium(III,IV) oxide by voltammetry. The deposition rate and cyclic voltammetric response of the electrodeposited material depend on whether the precursor complex contains a pentamethylcyclopentadieneyl (Cp*) or cyclopentadienyl ligand (Cp), and do not match, in either case, iridium oxide anodes prepared from non-organometallic precursors. Here, we survey our organometallic precursors, iridium hydroxide, and pre-formed iridium oxide nanoparticles. From electrochemical quartz crystal nanobalance (EQCN) studies, we find differences in the rate of electrodeposition of catalyst layers from the two half-sandwich precursors; however, the resulting layers operate as water-oxidizing anodes with indistinguishable overpotentials and H/D isotope effects. Furthermore, using the mass data collected by EQCN and not otherwise available, we show that the electrodeposited materials are excellent catalysts for the water-oxidation reaction, showing maximum turnover frequencies greater than 0.5 mol O_2 (mol iridium)$^{-1}$ s^{-1} and quantitative conversion of current to product dioxygen. Importantly, these anodes maintain their high activity and robustness at very low iridium loadings. Our organometallic precursors contrast with pre-formed iridium oxide nanoparticles, which form an unstable electrodeposited material that is not stably adherent to the anode surface at even moderately oxidizing potentials.

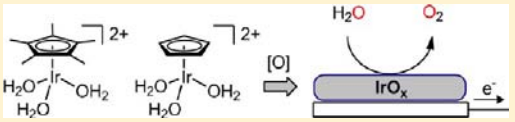

INTRODUCTION

Artificial photosynthesis, in which solar energy is captured and stored in the form of chemical bonds, holds promise for supplying future energy needs.[1] One of the key challenges in the generation and storage of such "solar fuel" is the need for an abundant and renewable source of reducing equivalents. Water is most often considered as the source; therefore, effective water-oxidation catalysts are needed to liberate electrons and protons, and in so doing, generate molecular oxygen (eq 1):

$$2H_2O \rightarrow O_2 + 4H^+ + 4e^- \quad (1)$$

Homogeneous, molecular metal complexes comprise one class of catalysts for this reaction. Remarkable progress has been made in recent years, with high turnover frequencies and longevity attained in certain systems with Group 7, 8, and 9 transition metals including manganese,[2] ruthenium,[3] cobalt,[4] and most recently, iridium.[5] However, myriad problems remain, including high electrochemical overpotentials, mechanistic ambiguities, and insufficient longevity for implementation in practical devices. Heterogeneous transition-metal oxides are the other major class of catalysts for water-oxidizing chemistry. Work in this area from Harriman, Grätzel, Nocera and others has shown that oxides of manganese, cobalt, ruthenium, and iridium are effective catalysts.[6−8] Among the catalysts known for water oxidation (WO), iridium oxides have the highest activities and turnover frequencies,[9] as well as excellent longevity and robustness, which has led to their use in commercially available proton-exchange membrane water electrolyzers.[10]

Iridium(IV) dioxide, having the rutile structure, is the most common oxide of iridium, and the only crystalline binary oxide known. An iridium(III) sesquioxide Ir_2O_3 can be prepared, but it is amorphous and thought to be impure in most preparations.[11,12] It has been reported to be superior to IrO_2 as a catalyst for WO,[6,13] though the lack of a crystalline form complicates analysis and introduces the potential for a strong dependence of the activity on the means of preparation.[14]

In the most common route to iridium oxide, aqueous hexachloroiridate is converted to colloidal iridium oxides by hydrolysis[15] or radiolysis.[16] The solutions are typically heated or aged, since hydrolysis of the $IrCl_6^{3-}$ anion is slow under neutral conditions. Accordingly, CV of fresh solutions of a simple iridium chloride precursor does not lead to electrodeposited oxide films. After hydrolysis, however, anodic polarization of an electrode in a solution containing nano-

Received: April 13, 2012
Published: June 22, 2012

   dx.doi.org/10.1021/ic300764f | Inorg. Chem. 2012, 51, 7749−7763

particles or iridium hydroxide does give deposition of nanostructured oxide material.[17]

Mallouk and co-workers have described the hydrolysis chemistry that gives rise to nanoparticles,[18] and recently reported data on the electrodeposition of an iridium oxide layer from an iridium hydroxide precursor.[19] The Murray group has recently reported that small, hydroxide-capped iridium oxide nanoparticles (**4**) are excellent catalysts for WO.[20] These recent studies complement earlier work that describes the material generated by such solution phase methods as primarily six-coordinate iridium in a highly disordered rutile structure.[16,21] Alternatively, iridium oxides can be generated directly by thermal decomposition of iridium salts in solution, on an electrode, or on a substrate surface, giving an active oxide.[22] Lower preparation temperatures give materials that are more amorphous and have higher activity for catalytic WO.[23]

Hydrous iridium oxide (Ir_2O_3) can also be prepared by oxidation of an iridium metal anode with an applied potential cycled between 0 and 1.5 V.[24] Iridium anodes were used at least as early as 1883.[25] These electrodes develop thick oxide layers and have very low overpotentials for WO.[13] Since the formation of this catalytic oxide is limited to iridium(0) surfaces, methods have been explored for initial electrodeposition of thin iridium metal surfaces, which can subsequently be converted to the oxide.[26] Other routes include sputtering to give iridium oxides with high WO activity.[27] The electrochromism of these materials[28] is associated with charging/discharging of the mixed-valence redox-active oxide.[29] The oxide layers are not ordered material,[29] but are instead, a highly disordered, amorphous hydrous oxide.[30,31]

Our own work has focused on a series of half-sandwich iridium complexes that are catalyst precursors for chemical and electrochemical WO. For complexes of the types {Cp*Ir(chelate)} and {CpIr(chelate)}, all current data suggest homogeneous catalysis at short times, although we cannot rule out contributions from heterogeneous material at longer times.[32,33] Rates for chemically driven WO with cerium(IV) have shown that oxidation of these catalysts is rate-determining and occurs in one-electron steps,[33] consistent with related complexes operating as diffusional electrocatalysts for electrochemical WO.[34] Chemical and electrochemical catalysis differ markedly, however, and each merits independent study.

In the absence of a chelate ligand, electrochemical oxidation gives a highly active heterogeneous catalyst for WO deposited on the cell anode. Specifically, we have reported deposition of $[Cp^*Ir(H_2O)_3]SO_4$ (**1**) to give a blue layer of amorphous iridium oxide material on the cell anode.[35] This result was prefigured by our previous work on cerium(IV)-driven catalysis with **1** which showed a greater than first-order dependence of oxygen evolution on the concentration of precursor.[33] In contrast, chelate ligands such as 2-phenylpyridine and bipyridine gave a first-order dependence on [Ir].[33] Thus, it seemed likely that dimerization or oligomerization of **1** gave a higher nuclearity species as the active catalyst. The heterogeneous material obtained by electrodeposition of **1** is completely amorphous, and contains a carbon admixture arising from oxidation of the Cp* in the precursor **1**.[36] This material is remarkably active for WO, and the catalyst continues to function for hours with essentially no deactivation.

We now report studies on thin layers of electrodeposited amorphous iridium oxide WO catalysts that are formed from organometallic precursors, namely, $[Cp^*Ir(H_2O)_3]^{2+}$ (**1**) and the new $[CpIr(H_2O)_3]^{2+}$ (**2**). These are somewhat similar to hydrous Ir_2O_3, but have distinct properties depending on the precursor employed. Furthermore, the materials deposited are electrochemically distinct from those deposited from solutions of iridium hydroxide **3** or iridium oxide nanoparticles **4**. The nature of the catalyst precursor affects the redox processes and behavior of the surface catalyst layers. Using an electrochemical quartz crystal nanobalance (EQCN) to monitor catalyst formation, we find striking differences in catalyst deposition rate between the organometallic complexes, iridium hydroxide, and pre-formed iridium oxide nanoparticles. This new method of probing catalyst formation with the EQCN provides information that has not been previously available and gives new insight into catalyst stability and activity. For the more stable materials generated from the organometallic complexes (**1** and **2**) or iridium hydroxide (**3**), the values of the overpotential and kinetic isotope effect for WO are indistinguishable among the three systems, suggesting similar mechanisms of action.

RESULTS

We previously showed that $[Cp^*Ir(H_2O)_3]SO_4$ (**1**) is a precursor for an amorphous electrodeposited iridium oxide catalyst.[35] We wondered if the activity of the resulting oxide film might depend on the organometallic ligand in the precursor and now investigate the corresponding Cp derivative (Figures 1 and 2). $[CpIr(H_2O)_3]SO_4$ (**2**) was prepared by

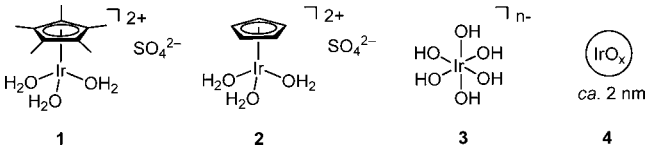

Figure 1. Iridium precursors used in this work.

treatment of the Cp iridium iodide polymer $[CpIrI_2]_x$ with silver sulfate in deionized water. Filtration, followed by removal of the solvent in vacuo, gave the product as a hygroscopic yellow solid. Repeated attempts to obtain single crystals for an X-ray diffraction study from saturated aqueous solutions gave a small number of thin yellow plates which we were able to characterize as $CpIr(H_2O)_2(O\text{-}SO_3)\cdot H_2O$. The sulfate ion is bound to the iridium through a single oxygen atom, unlike in the case of the Cp* analogue, which crystallizes with an outer-sphere sulfate.[34] The aqueous solution-phase speciation of **2** by NMR spectroscopy is complex, showing dependence on both the pH and sulfate ion concentration. $^{13}C\{^1H\}$ NMR spectra collected at pH 3 in D_2O show two signals at 71.4 and 73.7 ppm. The upfield signal is more intense in saturated Na_2SO_4 solution, but absent under strongly acidic conditions; $^{13}C\{^1H\}$ NMR in 1 M D_2SO_4 in D_2O gives a single signal at 73.8 ppm. (See Supporting Information, Figures S1−S6.)

Complex **2** is less soluble in dimethylsulfoxide (DMSO), in which it dissolves slowly to give a solution with a single ^1H resonance at 6.45 ppm and a single $^{13}C\{^1H\}$ resonance at 86.6 ppm. Crystals obtained by slow evaporation of a DMSO-d_6 solution of **2** show that two DMSO molecules replace the inner-sphere waters in **2** to give a *bis*-DMSO adduct $CpIr(S\text{-}DMSO)_2(O\text{-}SO_3)\cdot H_2O$. In both the aqua and the DMSO complexes of **2**, the sulfate is bound inner sphere, which in concert with the sulfate ion dependence of the NMR spectra, suggests that **2** might be best described as a mixed Cp iridium

dx.doi.org/10.1021/ic300764f | Inorg. Chem. 2012, 51, 7749−7763

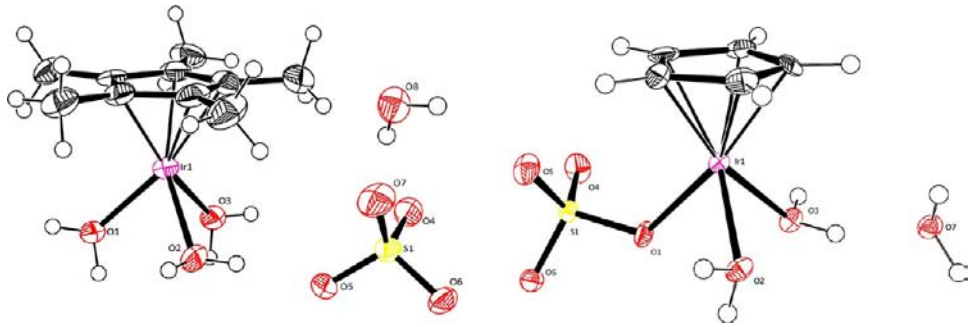

Figure 2. ORTEPs of the organometallic complexes **1**[34] (left) and **2** (right).

sulfate hydrate $CpIrSO_4 \cdot nH_2O$. For simplicity, however, we refer to it here by the hydrated form, $[CpIr(H_2O)_3]SO_4$.

Voltammetry. With compound **2** in hand, we set out to investigate its solution-phase electrochemical properties. The compound is soluble in aqueous solutions and at concentrations of between 1 and 3 mM gives solutions with a pH of approximately 2.90, a value comparable to **1** (pH 3.10 in the same concentration range).

As previously reported,[34,35] electrochemical oxidation of **1** induces deposition of a blue layer of heterogeneous material on the anode surface. The cyclic voltammogram showing formation of $\mathbf{BL_1}$ (that is, the layer formed from the Cp*Ir aqua complex **1**) is shown in the top panel of Figure 3. On the first anodic pass, only a strong anodic current response is seen. On the cathodic return, a new feature is observed which corresponds to an internal reduction event in the surface-bound layer. On the subsequent anodic pass, the associated internal oxidation event is observed. The catalytic feature appears more intense and onsets at a lower voltage on this second pass. On subsequent passes, both the pre-feature and the catalytic wave grow more intense as increasing amounts of electroactive material have been deposited.

A similar response is seen for compound **2**, as shown in the lower panel of Figure 3. On the first anodic pass, a strong catalytic current is seen. After multiple cycles of voltammetry, as for **1**, a pre-feature grows in intensity and corresponds to a quasi-reversible internal redox event of the surface-bound layer. There is an additional return, cathodic feature near 1225 mV that becomes more apparent on later cycles. This feature likely arises because of reduction of trapped high-valent iridium centers in the layer, and is not as pronounced in $\mathbf{BL_1}$. This may suggest that fewer of the sites in $\mathbf{BL_2}$ are solvent accessible and able to take part in water-oxidizing chemistry. Finally, compound **2** shows an onset of catalytic current on the first anodic pass at a potential that is about 100 mV more oxidizing than that seen for **1** (see Supporting Information, Figure S12). This is consistent with the complex having the less-donor Cp ligand being more difficult to oxidize than **1**.

The pre-feature assigned to the internal redox event of the catalytic layer is markedly different between $\mathbf{BL_1}$ and $\mathbf{BL_2}$. The differences in both the onset and the midpoint potentials for the pre-feature show that $\mathbf{BL_2}$ is easier to oxidize than $\mathbf{BL_1}$. Specifically, $\mathbf{BL_2}$ begins to be oxidized at about 400 mV vs NHE, compared to approximately 600 mV for $\mathbf{BL_1}$. The midpoint potentials of these processes for $\mathbf{BL_1}$ and $\mathbf{BL_2}$ differ by almost 100 mV ($E_{1/2}$ = 890 and 800 mV, respectively). The peak separation in both cases is about 59 mV; ideally, for a surface-bound species, the peak separation would be 0 mV. However, the pre-features and peak separation in the

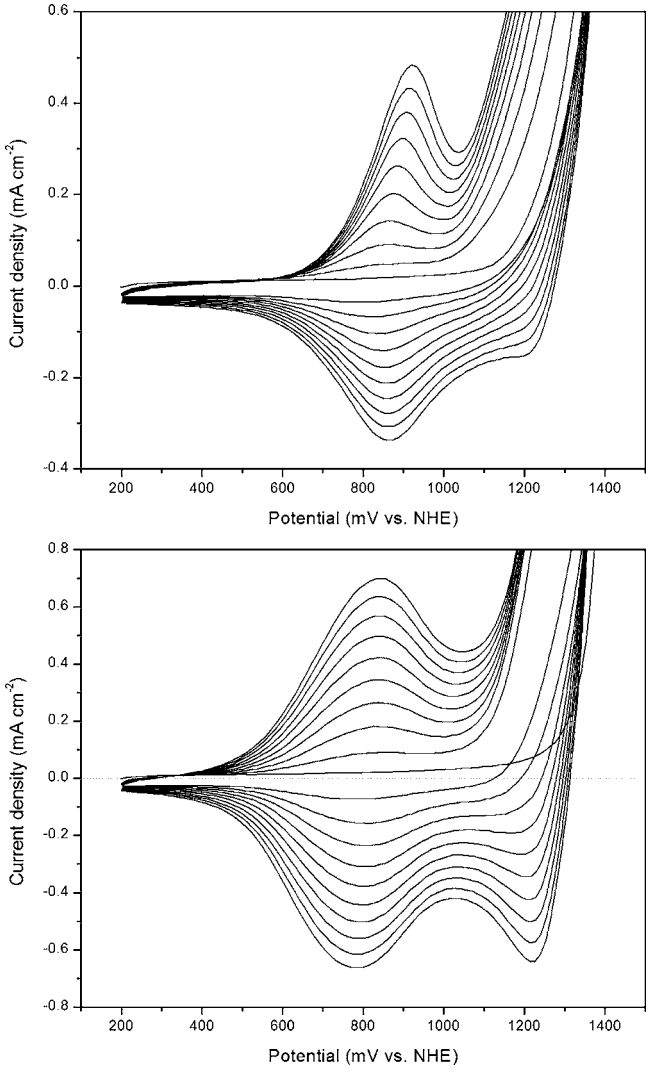

Figure 3. Cyclic voltammograms of compounds **1** (top panel) and **2** (bottom panel). Conditions: 1.72 mM **1** or **2** in 0.1 M KNO_3; pH about 3; scan rate: 50 mV/s; basal-plane graphite working electrode.

electrochemistry of $\mathbf{BL_1}$ and $\mathbf{BL_2}$ are qualitatively similar to that of electrochemically formed hydrous Ir_2O_3.[24]

Prolonged electrolysis of a solution containing precursor **2** results in the appearance of a blue layer on the electrode surface, similar to the case of **1**. The layer is visible within minutes, and continues to darken as more material deposits over time. Having observed the formation of this layer, we next

dx.doi.org/10.1021/ic300764f | Inorg. Chem. 2012, 51, 7749−7763

moved to compare BL_1 and BL_2 to layers prepared from other soluble precursors.

Mallouk et al. have recently investigated $[Ir(OH)_6]^{n-}$ as a precursor for the electrodeposition of iridium oxide on an anode for water splitting.[19] In their method, pulsed polarization of an electrode to oxidizing potentials in a solution containing hydrolyzed hexachloroiridate results in deposition of electrocatalytic iridium oxide material on the electrode surface. Since we have chosen to investigate electrodeposition with CV, we prepared iridium hydroxide according to Mallouk et al. but subjected the solution to cycling electrochemical oxidation as above for the molecular complexes **1** and **2**.

The solution-phase identity of the species "$[Ir(OH)_6]^{n-}$" (**3**) generated by hydrolysis is still a matter of debate. The material may be oligomeric, depending on the preparation, and it may contain either Ir(III) or Ir(IV), although evidence suggests that it is predominantly Ir(III).[37−39] The solution is pale yellow and does not show the presence of nanoparticles by TEM (in contrast to the case of related solutions of small, hydroxide-capped nanoparticles formed under similar conditions).

The cyclic voltammetry (CV) of the iridium hydroxide is shown below in Figure 4. On the first pass starting at 200 mV

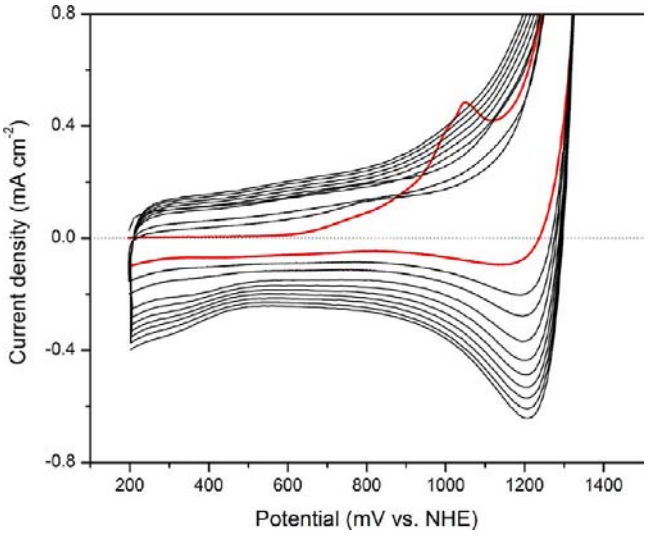

Figure 4. CV of a solution containing iridium hydroxide. The first scan is shown in the red trace, and the subsequent scans are shown in black. Conditions: [Ir] = 2 mM in 0.1 M KNO_3; pH 11; scan rate: 50 mV/s; basal-plane graphite working electrode.

vs NHE, there are no apparent oxidations up to about 600 mV. Starting at 600 mV, however, an increase in current is measured which likely results from multiple oxidation events. As in the case of the molecular precursors, an oxidation that is catalytic in appearance begins at the higher potential of 1100 mV. On the return cathodic sweep, there is a slight reduction feature at 1150 mV, but no other well-defined features down to 200 mV. On subsequent anodic cycles, the features between 600 and 1100 mV are no longer apparent. On subsequent cathodic scans, though, the return feature around 1200 mV increases in intensity; this is likely the result of reduction of trapped high-valent iridium species in the nascent surface layer. The voltammetry also becomes increasingly capacitative throughout the ten-cycle run shown in Figure 4.

The CV in Figure 4 contrasts with that of the molecular precursors **1** and **2**. The main difference is the lack of the quasi-reversible redox event seen for BL_1 and BL_2 around 891 and 801 mV, respectively, and responsible for the electrochromism of BL_1 and BL_2, behavior (vide infra) that provides an additional distinction between BL_1 and BL_2, and the layer generated from the purely inorganic **3**.

We were interested in comparing these properties with those of small hydroxide-capped iridium oxide nanoparticles **4** that have also been shown to form highly active catalyst layers. Murray et al. and Mallouk et al. have described preparations of **4**, and their preparation was used here.[18,20,40] We used CV for comparison between a solution containing **4** and the voltammetry of **1**−**3**. The results are shown in Figure 5.

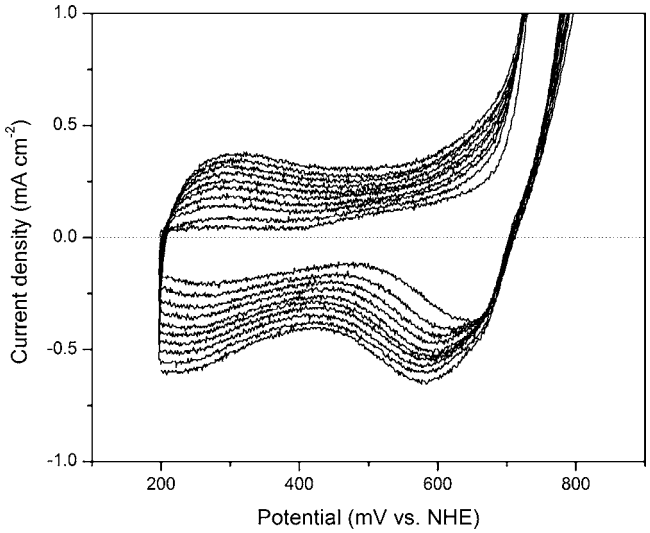

Figure 5. CV of a solution containing hydroxide-capped iridium oxide nanoparticles **4**. Conditions: [Ir] = 2 mM in 0.1 M KNO_3; pH 13; scan rate: 50 mV/s; basal-plane graphite working electrode.

On the first scan, the voltammetry of **4** is very similar to that of the iridium hydroxide **3**. Around 400 mV, there is onset of a broad irreversible oxidation followed by catalytic WO above 700 mV. This is likely lower than in the other cases because of the bulk solution pH of 13 required to stabilize the IrO_2 particles. On the return cathodic sweep, there is a return feature at around 650 mV, and a second around 275 mV. On the subsequent anodic scans, there is a new feature that grows more prominent around 300 mV. The catalytic wave and the cathodic features grow broader and more intense on each consecutive cycle. The quasi-reversible features growing around 300 mV and 600 mV are indicative of deposition of materials on the electrode that have internal redox events. Generally, the results are consistent with those found by Murray et al. for their films of electroflocculated small iridium oxide nanoparticles deposited by potential pulsing,[20] although the midpoint potentials that we find may be slightly different because of local pH effects from vigorous electrocatalytic WO.

EQCN. With these electrochemical data in hand, we were interested in gaining more information about the deposition process leading to the catalyst layers. From the voltammetry, it is clear that the deposited materials exhibit unique voltammetry in each case, but the dynamics of mass deposition at the electrode are an additional consideration not easily probed by simple voltammetry. In any large-scale solar-energy conversion, controlling catalyst deposition and composition will be important for cost considerations.

dx.doi.org/10.1021/ic300764f | Inorg. Chem. 2012, 51, 7749−7763

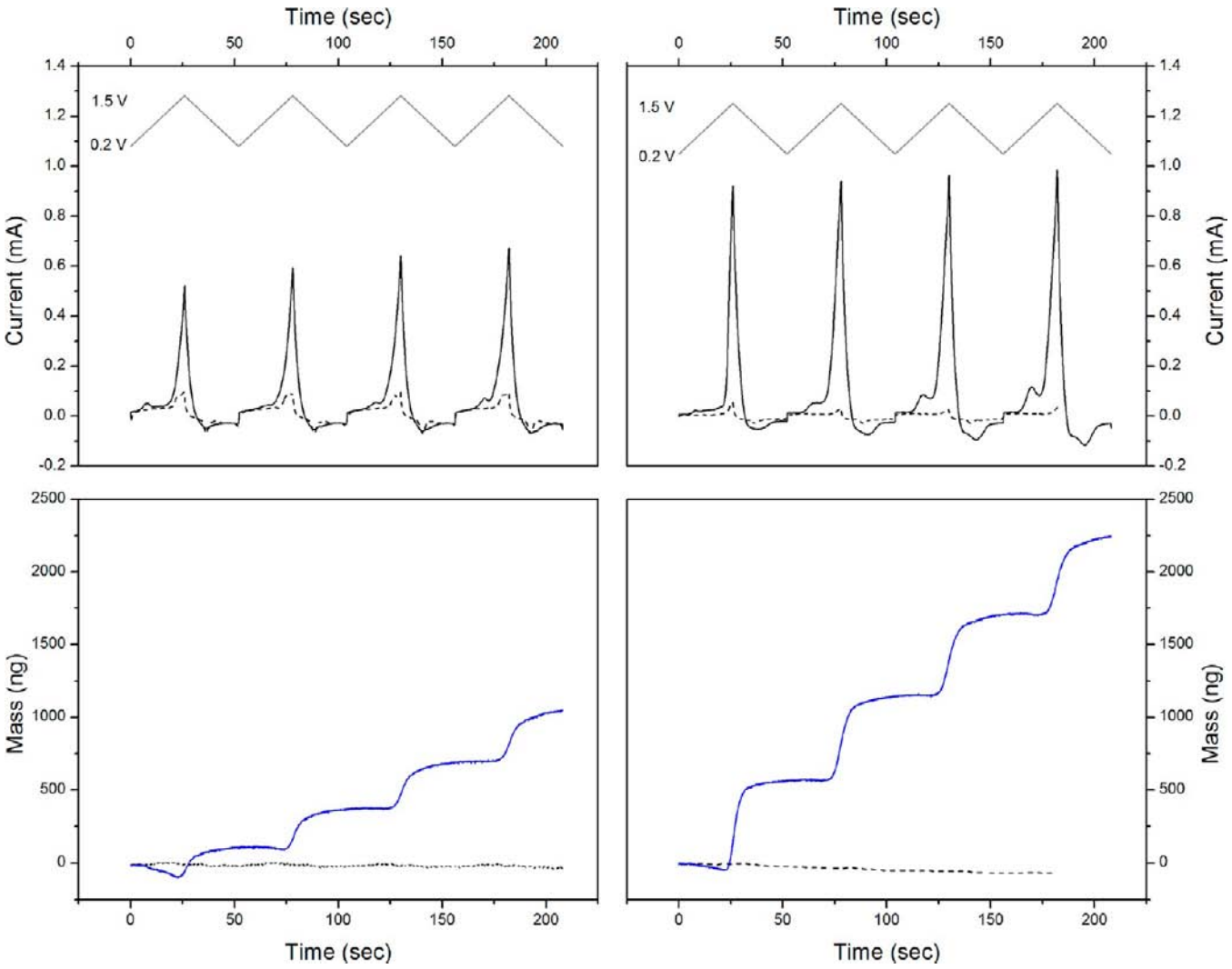

Figure 6. Comparison of current and mass responses of solutions containing compounds **1** (left panels) or **2** (right panels) as a function of time. Upper panels: gray lines represent applied potential; black solid lines represent current response of compounds **1** (left) or **2** (right) recorded by the potentiostat; black dashed lines are the background current. Lower panels: solid blue lines represent mass response in each experiment, while dashed lines are the corresponding metal complex-free backgrounds. Conditions: 0.1 M $LiNO_3$ in air-saturated deionized water; 1.72 mM **1** or **2**; pH about 3; scan rate: 50 mV/s; electrode material is sputtered gold on quartz.

In related work, we have recently developed a new method for monitoring homogeneous and heterogeneous WO catalysts by using an EQCN to monitor the electrode mass dynamically during catalysis and/or catalyst formation.[34] The change in mass is detected directly by measuring the resonant frequency of a gold-sputtered quartz crystal, which is related to the apparent mass of the crystal by the Sauerbrey equation.[41]

Here, we have monitored the electrode mass during voltammetry of solutions containing one of the precursors. The results are shown in Figure 6 for precursors **1** and **2**. In the first pass, as detailed earlier, each compound shows only a large anodic current with onset above 1 V. For **1**, the amount of current flowing on each pass increases markedly on each scan. For **2**, the increase in current on each scan is much less, but the total current flowing is greater. We also see that mass is only deposited above a threshold voltage in the voltammetry. The deposition has a step-function appearance, since mass is deposited only when the precursor complex is being oxidized.

The amount of catalyst deposited on each cycle for the two complexes is quite different. After four cycles of voltammetry, approximately 2245 ng of $\mathbf{BL_2}$ is deposited, while only 1044 ng of $\mathbf{BL_1}$ is deposited under analogous conditions. Thus, more than twice as much material (2.15×) is deposited in the case of the CpIr precursor complex. This shows that the organometallic ligand on the precursor complex strongly affects the kinetics of deposition of the heterogeneous catalyst. For **1**, the catalyst deposits increasing amounts of material on each cycle. For example, ∼100 ng of material is deposited on the first, and ∼260 ng on the second cycle. In contrast, the CpIr precursor **2** deposits ∼550 ng on each of the first four cycles of voltammetry.

The mass of the electrode during deposition of **1** and **2** was monitored for 24 cycles of voltammetry (See Supporting Information, Figure S13) over 20 min,[42] the first 12 cycles of which are shown in Figure 7. The mass deposited in the case of precursor **1** increases on each pass, whereas precursor **2** deposits progressively less mass on each cycle. At 10 cycles of voltammetry, the apparent electrode masses are the same, near 3300 ng. After approximately 16 cycles of voltammetry, the mass deposited on each cycle for both **1** and **2** is essentially

dx.doi.org/10.1021/ic300764f | Inorg. Chem. 2012, 51, 7749−7763

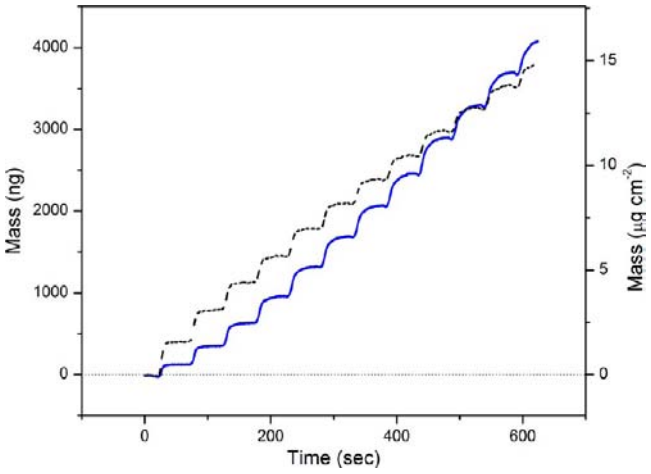

Figure 7. Electrode mass as a function of time over the first 12 cycles of voltammetry from 0.2 to 1.5 V. Conditions as described for Figure 6 and in Experimental Section. Blue solid line: mass of $\mathbf{BL_1}$; black dashed line: mass of $\mathbf{BL_2}$.

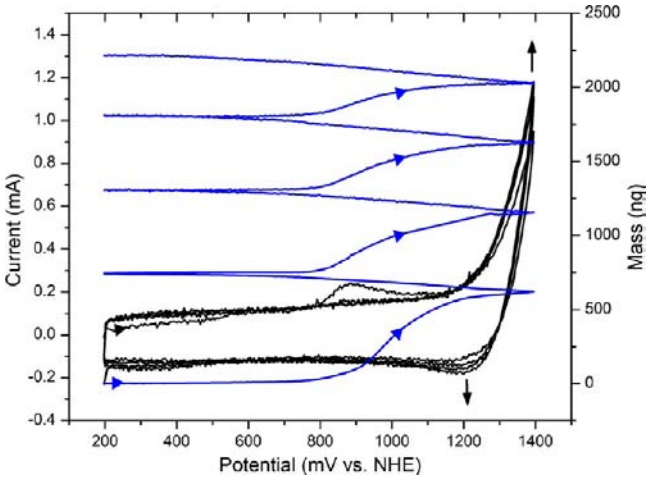

Figure 8. CV (black trace) and EQCN mass response (blue trace) of a solution containing iridium hydroxide **3**. Conditions: 0.1 M KNO_3 in air-saturated deionized water; [Ir] = 2 mM; pH 11; scan rate: 50 mV/s; electrode material is sputtered gold on quartz.

constant. However, the amount of material deposited from **1** is greater than for **2**. This implies a change in the kinetics of catalyst deposition during layer growth.

Increasing the solution concentration of the organometallic precursor results in an increase in the mass deposited on each cycle. This agrees with behavior we observe in bulk electrolysis, where thicker layers of $\mathbf{BL_1}$ form on the electrode surface when the concentration of precursor **1** is increased. Increasing the scan rate in the CV-driven deposition results in less mass per cycle, as less time is spent above the threshold voltage required for deposition. No differences have been observed in the behavior of anodes deposited at different scan rates. Differences have been seen in other work, however; cycles of oxidation and reduction can give higher activity manganese oxide versus constant-potential oxidation.[43]

We next compared the other precursors, the iridium hydroxide **3** and **4**. To ensure that they were stable under the conditions, the pH values of the solutions were kept at 11 and 13 for the iridium hydroxide and nanoparticles, respectively. These conditions are reported to keep each of the precursors stable, but likely contribute to the differences observed below.

The CV of **3** is shown along with the mass-response data from the EQCN versus applied potential in Figure 8. The electrochemistry is essentially the same as shown above in Figure 4; however, the larger surface-area electrode (gold on quartz) required for EQCN is employed in this case. The small anodic wave observed below 1 V is observed here as well, and, as before, only appears on the first scan. The catalytic wave and cathodic return feature around 1.2 V are also both present as before. The mass data over the same range clearly show that there is no change in the electrode mass below the potential of the irreversible oxidations around 700−800 mV. Upon passing through the oxidation feature, the electrode mass increases dramatically, depositing over 500 ng of material in the first anodic pass alone. The mass of the electrode continues to increase above 750 mV, but at a much slower rate over the first complete anodic/cathodic cycle. The slowing of deposition could be due to either (1) bubble formation during catalytic WO, which interferes with electrode mass measurement, or (2) depletion of precursor from the diffusion limit of the electrode surface resulting in less material being deposited.[41]

The results on the small, hydroxide-capped iridium oxide nanoparticles (**4**) in Figure 9 are remarkably different than the

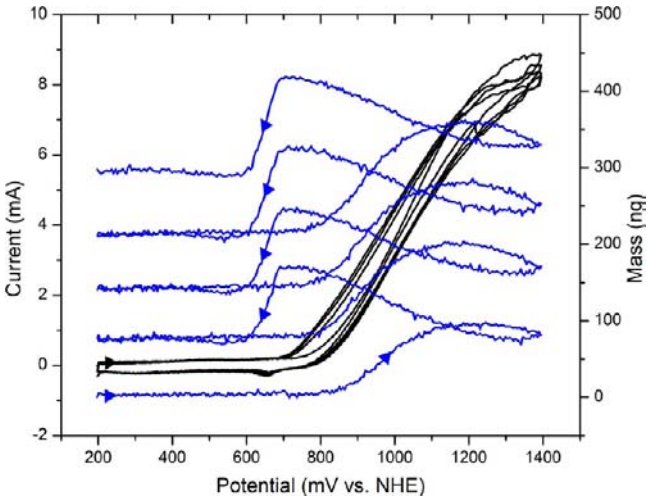

Figure 9. CV (black trace) and EQCN mass response (blue trace) of a solution containing hydroxide-capped iridium nanoparticles **4**. Conditions: 0.1 M KNO_3 in air-saturated deionized water; [Ir] = 2 mM; pH 13; scan rate: 50 mV/s; electrode material is sputtered gold on quartz. The desorption of the nanoparticles takes place at 650 mV in the cathodic pass.

results on any of the other materials. On the first anodic scan, only a very strong, catalytic response is observed with onset around 700 mV at pH 13. This agrees well with the results obtained on basal-plane graphite in Figure 5. At about 650 mV on the return cathodic scan, there is a fairly narrow reduction feature, which may be paired with a broader feature observed in the data on basal-plane graphite.

The mass data show that at about 800 mV vs NHE, mass is deposited as long as the voltage is above 600 mV on the first cycle. (The data likely are affected by bubble formation— a source of error—but the data seem consistent with the deposition seen by Murray et al.) However, once the voltage

dx.doi.org/10.1021/ic300764f | Inorg. Chem. 2012, 51, 7749−7763

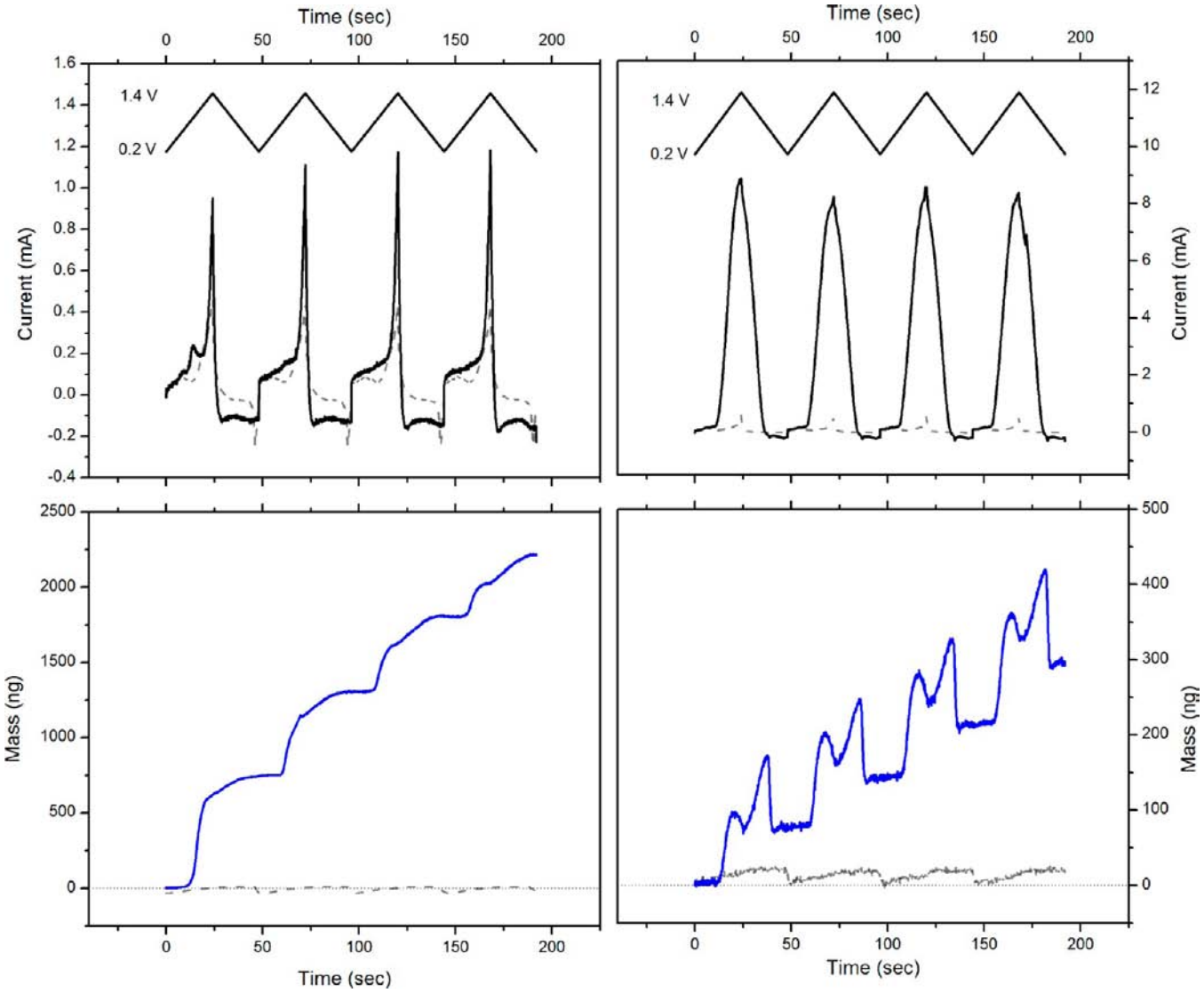

Figure 10. Comparison of current and mass responses of solutions containing 2 mM iridium in the form of iridium hydroxide (left panels, pH 11) or hydroxide-capped iridium oxide nanoparticles (right panels, pH 13) as a function of time. Upper panels: black lines represent applied potential; black solid lines represent current response as recorded by the potentiostat; gray dashed lines are the background current. Lower panels: solid blue lines represent mass response in each experiment, while dashed lines are the corresponding iridium-free backgrounds. Conditions: as described in captions for Figures 8 and 9. Reversible uptake for **4** is again apparent in the lower right panel.

reaches about 650 mV on the cathodic pass, there is a marked decrease in the electrode mass; this represents loss of some of the material from the surface. Bubble formation can also be detected as an *apparent* mass loss, as discussed by Buttry and Ward,[41] and we believe this is responsible for the apparent mass loss between 1200 and 1400 mV, the region of most vigorous oxygen evolution with consequent formation of bubbles.

Murray's original report[20] on layers formed from **4** did not discuss the stability of the anodes. Mallouk et al. have found that these layers are unstable, especially in comparison with those formed from iridium hydroxide.[19] The data shown here strongly suggest that one contribution to the instability of the films, especially at low loadings of catalyst, involves reduction of at least some iridium sites in the deposited material. This may result in protonation of oxo-bridges, thus weakening the connection to the surface, and allowing dissolution of iridium. This could happen during storage of the anode, or during a catalytic cycle.

A direct comparison of the EQCN data for the iridium hydroxide and small iridium oxide nanoparticles is shown above in Figure 10. In spite of the difference in pH of the bulk solutions, 11 and 13, respectively, several key comparisons can be made. Both electrodes uptake material at the same voltage of about 800 mV. Additionally, both preparations plateau in mass after some time above this voltage, but continue to deposit on subsequent cycles. However, the amount of material adherent to the electrode surface in the case of **4** is much smaller. This could be due to competition between deposition processes and vigorous oxygen evolution under the conditions (pH 13), or simply a difference in the population of species that can deposit in the two cases. If there is a speciation of the nanoparticles, then the first step in formation of the electroflocculated films could be deposition of some material other than particles of **4** themselves. This may be consistent with a small amount of iridium hydroxides being present in solution, since the potential of mass deposition onset matches qualitatively between the two cases.

dx.doi.org/10.1021/ic300764f | *Inorg. Chem.* 2012, 51, 7749−7763

Several broad comparisons can be made from EQCN between the cases of **1** versus **2**. In the case of $\mathbf{BL_1}$ and $\mathbf{BL_2}$, there are no changes in the mass of the anode below the deposition potentials. This suggests that the films, even as thin submicrogram layers, are stable at potentials where they are in their reduced form, which matches previous reports on the stability of hydrous iridium oxide (Ir_2O_3) layers under reducing conditions.[44] This behavior contrasts with the layer generated from small nanoparticles, which clearly partially desorb or dissolve from the electrode at a potential below 600 mV. Although this could be a result of the pH conditions, it is problematic for storage or use of electroflocculated nanoparticle films under nonoxidizing conditions. However, the materials generated from **1**−**3** seem to be reductively stable down to 200 mV. Interestingly, the CpIr precursor **2** and iridium hydroxide **3** both deposit around 2250 ng of material at the chosen concentration (with all parameters identical, except for bulk pH). However, the Cp*Ir precursor **1** only deposits about 1000 ng under the same conditions. This could be due to higher lability of the cyclopentadienyl ligand versus the pentamethylcyclopentadienyl ligand or an inhibitory effect of the larger organic ligand.

Oxygen Evolution Studies. In previous work,[35] we monitored oxygen evolution with a thick layer (1−2 μm) of $\mathbf{BL_1}$ on the electrode surface. We found essentially quantitative conversion of water into dioxygen after a short induction period during which no oxygen was produced. We assign this induction period to a charging process in the layer itself; during charging, the electroactive iridium sites in the thick layer are oxidized, likely propagating from the electrode to the catalytically active sites that have solvent accessibility. This process complicates the data analysis, and adds ambiguity as to the fate of the first redox equivalents transferred into the catalyst layer upon initiating water electrolysis. Very thin layers of catalyst that we use here show reduced capacitance and charging, simplifying the interpretation of the results. In a representative experiment, a thin layer of $\mathbf{BL_2}$ was electrodeposited onto a gold working electrode with ten cycles of voltammetry between 0 and 1.5 V at 50 mV/s. This experiment deposits an active catalyst layer that is seen by voltammetry and corroborated in the above experiments with the nanobalance, but is invisible to the naked eye. The electrode was then transferred to the oxygen-detection apparatus[45] containing an aqueous solution of 0.1 M KNO_3 at pH 6, and the system was allowed to equilibrate before initiating electrolysis. At time zero (see Figure 11), the electrode was polarized to 1.4 V, and an increase in the oxygen concentration in the solution was detected by the Clark electrode. The current quickly reaches a steady value, and the oxygen concentration continued to rise. After 10 minutes of continuous electrolysis, the electrode was deliberately depolarized, and the oxygen concentration stopped rising. With this low catalyst loading, oxygen evolution commences immediately following polarization of the electrode, and the oxygen evolution rate is constant. This implies that the catalyst layer is stable, and that the catalytic activity does not markedly change on the time scale of this experiment.

A comparison of the oxygen evolution activity of $\mathbf{BL_1}$ and $\mathbf{BL_2}$ under the same conditions is shown in Figure 11. As previously found for $\mathbf{BL_2}$,[35] oxygen evolution with a thin layer of $\mathbf{BL_2}$ deposited over 10 cycles of voltammetry is essentially quantitative from transferred current.

The rates of oxygen evolution for the two catalysts can be compared at this point based on the yield of oxygen per unit time, and on an electrode surface area basis (in this case, a gold working electrode with surface area of 0.017 cm^2). In the case of $\mathbf{BL_1}$, oxygen is evolved at a rate of 14.5 nmol O_2 sec^{-1} cm^{-2}. For $\mathbf{BL_2}$, oxygen is evolved at a slightly greater rate of 17.9 nmol O_2 sec^{-1} cm^{-2}. From the EQCN mass data, it is also possible to convert these rates into turnover frequencies. Assuming that the organometallic precursors are deposited such that they take all the carbon in their ligands onto the surface with them, an estimate for catalytic rate on a per-iridium basis can be calculated. After the 10 cycles of voltammetry used to deposit the catalyst, the anode likely has about 216 ng of material on the gold electrode surface by extrapolation from the EQCN data. Using the molecular weights of the precursor complexes and the other relevant data gives 0.567 nmol and 0.695 nmol of iridium for $\mathbf{BL_1}$ and $\mathbf{BL_2}$, respectively, corresponding to turnover frequencies of 0.54 and 0.35 turnovers sec^{-1} for $\mathbf{BL_1}$ and $\mathbf{BL_2}$. As it is unlikely that the entire carbon containing ligand is incorporated into the thin catalyst layer or that all iridium atoms are involved in the catalysis, these turnover frequencies represent a very conservative estimate.[46]

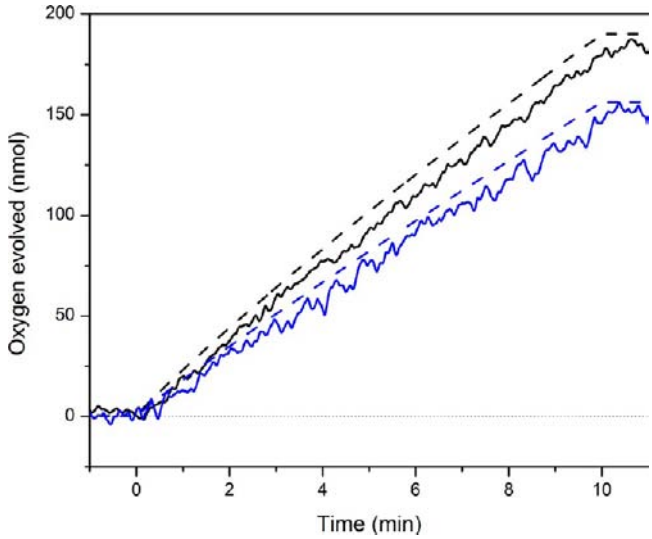

Figure 11. Oxygen generation by $\mathbf{BL_2}$ (black) and $\mathbf{BL_1}$ (blue) as monitored by Clark-type oxygen electrode. The working electrode was polarized to 1.4 V vs NHE at time zero, and the potential was turned off after 10 minutes. No oxygen is produced in the absence of catalyst. Conditions: 0.1 M KNO_3 in air-saturated deionized water; gold working electrode. Solid black and blue lines: detected yield of O_2 based on Clark-electrode data; dashed black and blue lines: predicted yield from charge transferred.

Morphology of the Deposited Materials. Analysis of the deposited oxides for differences in apparent morphology was conducted by scanning electron microscopy (SEM). Representative SEM images of the catalyst layers are shown in Figure 12. In both cases, a catalyst layer was deposited at 1.4 V for 40 min on an FTO-coated glass slide. This deposition time is long enough to provide a complete, thick coverage of the FTO surface suitable for imaging. In the case of both $\mathbf{BL_1}$ and $\mathbf{BL_2}$, the catalyst appears as a highly nanostructured surface, resembling a cauliflower; some cracking also occurs on dehydration of the film in the high-vacuum chamber.[47] In the case of $\mathbf{BL_1}$, the nanostructures are quite small, on the order of 100 nm or less, while $\mathbf{BL_2}$ has somewhat larger 200−300 nm nodules.

dx.doi.org/10.1021/ic300764f | Inorg. Chem. 2012, 51, 7749−7763

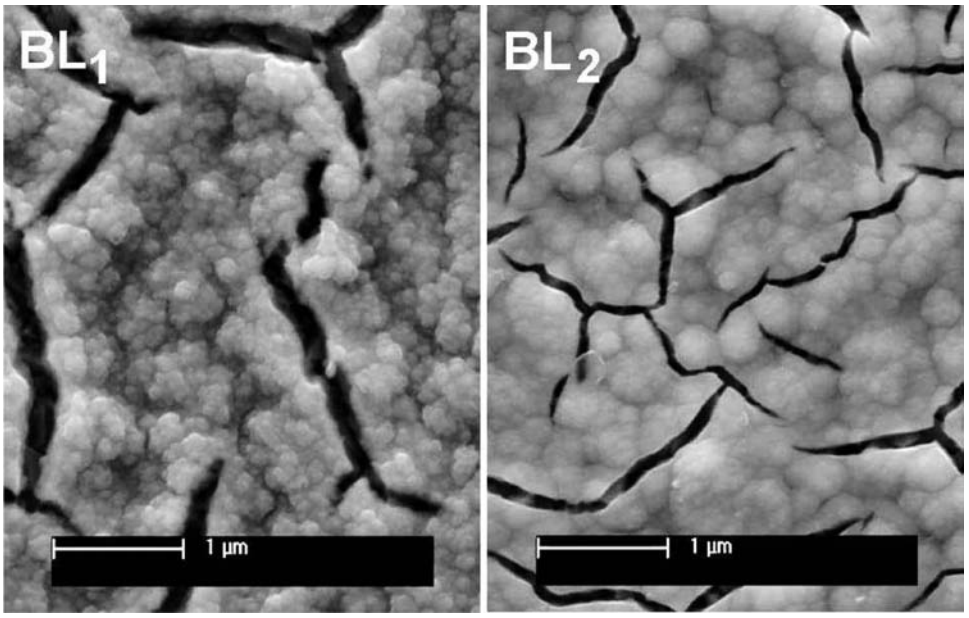

Figure 12. Top-view SEM image of BL_1 (left panel) and BL_2 (right panel) deposited onto FTO-coated glass. The catalyst layers were deposited from 1.72 mM solutions of **1** or **2** at 1.4 V for 40 minutes. The cracks result from layer dehydration in the SEM vacuum chamber.

Despite the apparent difference in nodule size between thick layers of BL_1 and BL_2, the two layers have similar apparent electrocatalytic WO activity. Thick layers of BL_1 and BL_2 on FTO prepared analogously to those imaged by SEM were rinsed and transferred to a fresh solution of 0.1 M potassium nitrate at pH 3.3 and polarized to 1.4 V vs NHE. The steady-state currents for both anodes were measured after a dwell time of 5 min to compensate for charging effects. For BL_1, the steady-state current density was 2.4 mA cm^{-2}, whereas for BL_2 the current density was 2.05 mA cm^{-2}. This represents a 15% greater current density for the layer deposited from the Cp*Ir precursor versus the CpIr precursor, which is different from what is seen with very thin layers in which BL_2 is superior (vide supra). The difference in apparent surface morphology between BL_1 and BL_2 likely stems from the different organometallic precursor employed, further demonstrating the role of the organic ligand fragment in heterogeneous catalyst formation in these systems.

Annealing. The catalyst layers formed by electrodeposition of solutions of **1**, **2**, and **3** are amorphous as determined by powder X-ray diffraction. On heating above 400 °C in air, however, peaks assigned to rutile IrO_2 appear. Annealing was accomplished by subjecting a series of BL_1- or BL_2-coated FTO glass slides to temperatures of 400 °C, 500 °C, or 600 °C for 2 h in air. In the cases of both layers, the annealing data show the growth of the crystalline iridium dioxide upon heating, especially at the higher temperatures (see Supporting Information, Figures S9–S11). After annealing, the layers change from their characteristic blue colors to an opaque, gray-black. Similar annealing behavior has been observed for iridium oxide films grown by anodic cycling or sputtering of iridium metal.[48]

The annealed films display very different electrochemical properties. CV of a platinum disk electrode coated with BL_1 before and after annealing at 600 °C is shown in Figure 13.

Annealing causes two marked changes in the electrochemistry. First, the catalytic wave which onsets around 1.3 V in the annealed layer is much less intense at the same potential

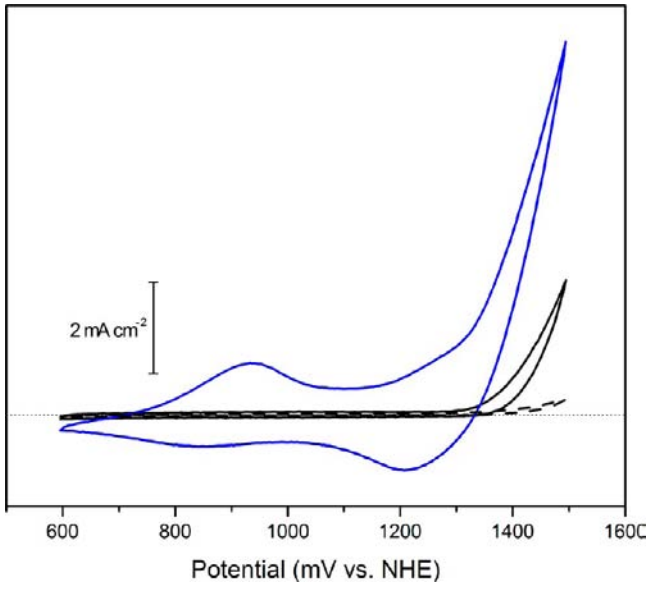

Figure 13. Comparison of CV of BL_1 before (blue) and after (black) annealing at 600 °C for 2 h. Conditions: 0.1 M KNO_3 in air-saturated deionized water; scan rate: 50 mV/s; platinum-disk working electrode.

than the catalytic response in the layer as deposited. This is likely due to a loss in solvent-accessible surface area and a decrease in the number of sites active for WO. Second, the quasi-reversible precatalytic feature at 900 mV in the amorphous layer is totally absent in the annealed layer. This indicates that there is essentially no internal redox chemistry of crystalline iridium dioxide at these voltages, and that the film is no longer highly capacitive. Importantly, the thin iridium dioxide layer has metallic conductivity (ca. 10^4 Ω^{-1} m^{-1}) comparable to basal-plane graphite (10^2 Ω^{-1} m^{-1}) or platinum (10^6 Ω^{-1} m^{-1}), which in concert with the lack of redox chemistry, results in the iridium oxide catalyst being essentially unobservable by electrochemistry except for the catalytic response leading to oxygen evolution.[49]

dx.doi.org/10.1021/ic300764f | Inorg. Chem. 2012, 51, 7749–7763

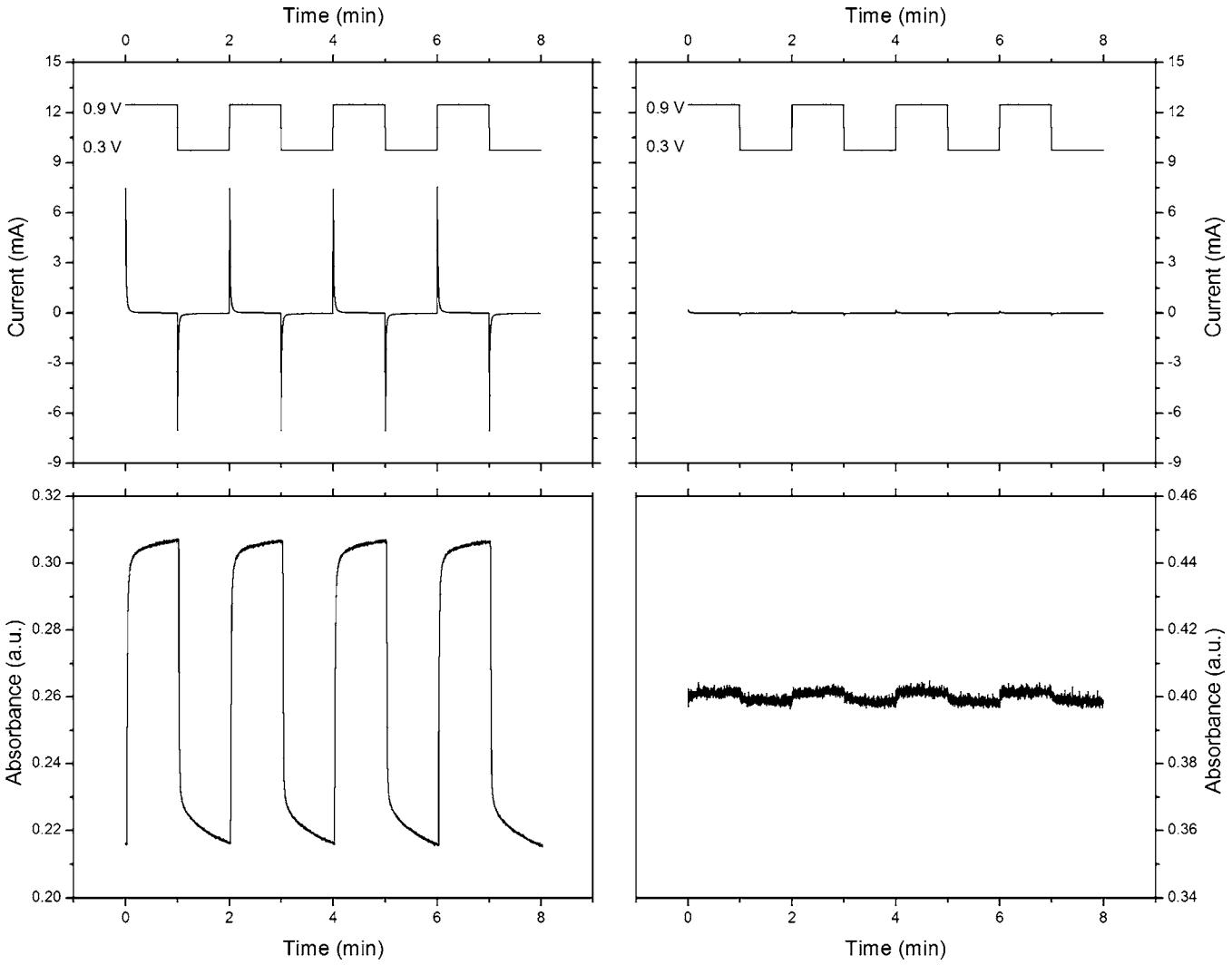

Figure 14. Electrochromism data for $\mathbf{BL_2}$ before (left panels) and after (right panels) annealing to form crystalline IrO_2. Conditions: 0.1 M KNO_3 in air-saturated deionized water; electrochemistry was conducted in a spectrometer cuvette as described in the Experimental Section. Absorbance measured at 580 nm.

Electrochromism. The quasi-reversible redox feature in $\mathbf{BL_1}$ and $\mathbf{BL_2}$, lost on annealing, is associated with a potential-dependent color change in the bulk layer between light yellow-green when reduced and dark blue when oxidized.[35] It seemed likely that the loss of the redox feature would be accompanied by reduced electrochromic behavior as well. UV−visible spectroscopy on layers less than 0.5 μm thick deposited from a 1.72 mM precursor solution onto transparent FTO glass show that the λ_{max} of the oxidized form in the visible region of the spectrum is about 580 nm, as observed previously with many iridium oxide materials.[50] (See Supporting Information for spectra, S17.) This 580 nm band has recently been discussed by Osterloh et al., and can be involved in visible light-driven photocatalytic WO.[51]

After rinsing and immersion in 0.1 M KNO_3, spectroelectrochemistry was performed when alternating potentials above and below the reversible redox event were applied (0.3 and 0.9 V) while the absorbance at 580 nm was monitored in real time. Representative data are shown in Figure 14 for the case of $\mathbf{BL_2}$. As the potential is cycled, the layer changes color between deep blue and greenish yellow, as monitored by the absorbance change at 580 nm. On consecutive cycles, the same changes are recorded, with little variation in the maximum and minimum absorbance values, consistent with the redox changes being completely reversible. Most importantly, there is no UV−visible spectroscopic evidence for loss of material from the electrode surface on reduction, in agreement with the stable mass behavior observed by EQCN at potentials below 0.9 V (see above).

After annealing, there is a remarkable change in the electrochromism of the layers. As described above, the reversible precatalytic feature is lost in the case of $\mathbf{BL_1}$ and $\mathbf{BL_2}$. Annealing also results in near complete loss of the electrochromic properties of the layer. These results are shown in the right panels of Figure 14. Specifically, as the potential is cycled as before, there is essentially no change in the color of the electrode. Results for $\mathbf{BL_1}$ were similar to those obtained for $\mathbf{BL_2}$, and these results are included in the Supporting Information, Figures S15 and S18.

For the material generated by deposition from solutions of **3**, the results showed very different absorbance properties in the UV−vis region. (See Supporting Information for spectrum of the layer (Figure S19) and bleach kinetic traces (Figure S16).) First, the dominant peak found at 580 nm for the **BL** materials

dx.doi.org/10.1021/ic300764f | *Inorg. Chem.* 2012, 51, 7749−7763

is completely absent, and instead, only a very broad feature at about 700 nm is observed. Furthermore, the layer is much less electrochromic. While there is a slight change in absorbance at 580 nm, it is much less dramatic than in the case of the layers deposited from **1** and **2**. Thus, the organometallic precursors offer a route to highly electrochromic and redox-active electrodeposited films not available by electrodeposition of classical inorganic materials. Indeed, most previous studies of electrochromic iridium oxides required exotic methods to prepare the electrodes or observe the electrochromism because of the paucity of methods for generating electrochromic layers on transparent substrates.

Overpotential for Oxygen Evolution. An important metric for assessing the efficiency of WO catalysts is the overpotential required to reach a particular rate above the thermodynamic potential for WO. The overpotential of a thick deposit of $\mathbf{BL_1}$ for WO has been estimated previously;[35] however, for a comparative study with other materials, different conditions are used here. As before, a current density of 0.5 mA cm^{-2} is used as the point of comparison.

To minimize the influence of local pH, bubble formation, and mass transport effects, a rotating-disk electrode was used. A layer of catalyst (ca. 3 μg) so thin that it is not even visible to the eye was deposited on the anode (as above with 10 cycles of voltammetry), the electrode was rinsed, and then transferred to pH-adjusted solutions of 0.1 M KNO_3 and the steady-state current at multiple potentials was measured to obtain a Tafel plot (dwell time: 5 min.).

Between pH 1.2 and 4.2, the overpotential for $\mathbf{BL_2}$ is invariant, having a value of 240 ± 10 mV (see Supporting Information, Figure S20). Above pH 4.2, the overpotential increases progressively with pH. (e.g., at pH 6.10, it is 345 mV.) This behavior could be better controlled by inclusion of a buffer, which will be described in a future report. However, for the experiments here on comparing the various iridium materials, pH 3.3 is used since it is in the pH-dependent range for $\mathbf{BL_1}$ and $\mathbf{BL_2}$ and, furthermore, is a relevant pH for applications of the catalysts in PEM-type devices.

Catalyst samples were prepared in a similar fashion with 10 cycles of voltammetry to ensure comparable numbers. For $\mathbf{BL_1}$ and $\mathbf{BL_2}$, anodes were deposited with 6.5 nmol and 8.0 nmol of catalyst, respectively. For **3**, approximately 2.6 nmol of iridium was deposited. To prepare the sintered sample of $\mathbf{BL_2}$, which is essentially crystalline iridium dioxide (see above), an identical layer of 6.5 nmol $\mathbf{BL_1}$ was deposited onto a platinum disk, sintered on the platinum, and then the Tafel data collected under identical conditions to the other samples.

The current densities as a function of applied potential for $\mathbf{BL_1}$, $\mathbf{BL_2}$, and the catalyst derived from **3** are shown in Figure 15. $\mathbf{BL_1}$ and $\mathbf{BL_2}$ have essentially indistinguishable overpotentials of 240 ± 10 mV. This is not unexpected, as the two materials are generated by similar methods and from similar precursors. Surprisingly, the layer generated by deposition of iridium hydroxide also has an overpotential of 240 mV that is nearly indistinguishable from $\mathbf{BL_1}$ and $\mathbf{BL_2}$. Thus, these very thin layers of amorphous iridium oxide are comparable in terms of activity. The annealed material has a very different overpotential for WO. The catalyst shows essentially no activity above the background of the platinum disk electrode even at potentials as high as 1.5 V; the overpotential required to reach 0.5 mA cm^{-2} is 490 mV. This is a large difference, and highlights the remarkable benefit of using amorphous iridium oxide materials.

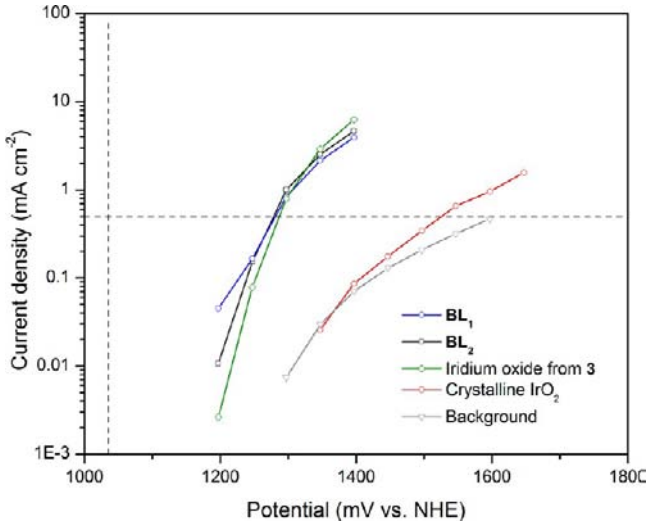

Figure 15. Tafel Plots for the iridium oxide materials discussed in this work. Conditions: 0.1 M KNO_3 in air-saturated deionized water; pH 3.3; $E^{\circ\prime}$ = 1035 mV vs NHE; dwell time: 5 min; platinum-disk working electrode rotating at 1500 rpm. Blue trace: $\mathbf{BL_1}$; black trace: $\mathbf{BL_2}$; green trace: layer generated from **3**; red trace: annealed $\mathbf{BL_1}$ (crystalline IrO_2); gray trace: Pt-electrode background; vertical dashed black line: thermodynamic potential for WO at this pH ($E^{\circ\prime}$); horizontal dashed black line corresponds to 0.5 mA cm^{-2}.

From the EQCN mass data, the current densities from the Tafel plots can be converted into estimated turnover frequencies for the layers. For $\mathbf{BL_1}$, this is 0.31 turnovers sec^{-1} at 1.4 V. This compares well with the values obtained for the same catalyst on a gold electrode (see above). For the annealed material, though, the turnover frequency at 1.6 V (an overpotential of 0.57 V) is only 0.08 turnovers sec^{-1}.

The overpotential changes depending on the thickness of the layer. Anodes coated with $\mathbf{BL_2}$ from 10-cycle, 20-cycle, and 30-cycle depositions of catalyst prepared by CV in solutions of **2** were compared (see Supporting Information, Figure S21). For the 20-cycle layer, the overpotential drops to ~215 mV from 240 mV for the 10-cycle layer. The 30-cycle layer offers a further improvement in the overpotential, dropping to ~200 mV. This is in excellent agreement with our previously published results on thick layers at pH 3 for $\mathbf{BL_1}$.[35] Because we are comparing overpotentials by normalizing to the geometric surface area of the electrode, higher catalyst loadings will give lower overpotentials, consistent with the presence of more catalytic sites.

H/D KIE for Oxygen Evolution. Because $\mathbf{BL_1}$, $\mathbf{BL_2}$, and the layer deposited from iridium hydroxide had comparable overpotentials for WO, a similar mechanism is likely to operate. To probe this, the H/D kinetic isotope effect (KIE) was measured for each case. Typically, secondary isotope effects with values greater than unity are observed in WO, which is consistent with the turnover-limiting step of the catalytic cycle involving formation or reaction of an active high-valent intermediate. For *cis,cis*-$[Ru(bipy)_2(H_2O)_2]O^{4+}$, a KIE of 1.7 has been found for the reaction in which O−O bond formation is the rate-determining step.[52] For most systems, including our own $[Mn(terpy)(H_2O)O]_2^{3+}$, rate-limiting oxidation of the catalyst to form the high-valent species is observed. In the case of $[Mn(terpy)(H_2O)O]_2^{3+}$, a KIE of 1.64 was found experimentally.[53] Our results on mononuclear iridium WO catalysts in both chemically and electrochemically driven cases

dx.doi.org/10.1021/ic300764f | Inorg. Chem. 2012, 51, 7749−7763

are also consistent with rate-determining catalyst oxidation.[33,34] For iridium oxides, we are aware of only one study which examined the H/D KIE on oxygen evolution. In a 2004 report from Mallouk et al., no change in rate of oxygen evolution was found for colloidal iridium oxide in H_2O versus D_2O, when oxidized with $[Ru(bpy)_3]^{3+}$.[54] Thus, the KIE in this case is 1.0, which is consistent with rate-limiting oxidation of the catalyst by the outer-sphere oxidant. We are unaware of any previous reports of H/D isotope effects on oxygen evolution with electrochemically driven iridium oxide materials.

The rate of oxygen evolution with either H_2O or 99.9% D_2O was measured at an applied voltage of 1.2 V vs NHE with a rotating-disk electrode in 0.1 M KNO_3. For $\mathbf{BL_1}$, the H/D KIE is 2.68 ± 0.16, and for $\mathbf{BL_2}$ the KIE is 2.72 ± 0.20. These two values are indistinguishable within the error, which strongly suggests that the mechanism of WO is identical in each case despite the differences in the voltammetry of $\mathbf{BL_1}$ and $\mathbf{BL_2}$. The layer deposited from iridium hydroxide **3** has an H/D KIE of 2.88 ± 0.49. This suggests that the three layers, despite being generated from different soluble precursors share a common active site and mechanism of action. This result agrees well with recent reports of the observation of a hydroperoxide intermediate in WO with $[Ru(bpy)_3]^{3+}$ as the oxidant.[55]

DISCUSSION

Electrodeposited iridium oxide materials are perhaps the best WO catalysts known at present, having both a low overpotential and high chemical and mechanical stability. Of the two classes of binary iridium oxides, Ir_2O_3 and IrO_2, Ir_2O_3 offers the better opportunity for diversity in the materials and optimization of their catalytic activity by varying the method of preparation. Here we show that modification of the organometallic ligand in a soluble precursor to iridium oxide makes a significant difference in the deposition process and the properties of the electrodeposited material. The catalyst layers obtained from **1** and **2** can be deposited in a controlled way to give layers of varying thickness. They have a low overpotential for WO even at a surface loading on the order of nanomoles cm^{-2}. Additionally, because the precursors **1** and **2** are stable at acidic pH values that cause **3** and **4** to precipitate, it is possible to prepare stable anodes with very thin layers of iridium oxide under widely varying solution conditions. Indeed, we have previously shown that essentially identical layers can be deposited from acidic solutions of **1** and basic solutions of the related dimer $[(Cp^*Ir)_2(OH)_3]OH$, which forms from **1** at high pH.[35]

Organometallic ligands are not strictly required for high activity though, as Mallouk et al. have shown.[19] Iridium hydroxide, obtained via careful hydrolysis of hexachloroiridate can be electrodeposited in a fashion similar to **1** and **2**. However, the behavior of the solution during the deposition process is quite different. Since iridium hydroxide is very sensitive to pH effects, iridium hydroxide precipitates and flocculates in the electrochemical cell during deposition of surface-bound layers. Thus, at the end of a deposition run (such as those used here for preparing FTO-glass slides with iridium oxide), there is a large amount of iridium oxide at the bottom of the cell neither stably attached to the anode nor remaining soluble in solution for future depositions. This observation is confirmed by the EQCN results for precursor **3** shown in Figures 8 and 10; the deposition rate slows progressively in time, even on the short time scale investigated here.

The advantage of our solutions of **1** or **2** is that they can be used multiple times to generate up to 10 thick films (thickness: 2 μm; area: 4 cm^2; on FTO-coated glass) from one solution (20 mL, containing 16 mg of **1**) with little change in the chemistry of the deposited material. Accordingly, despite the high cost of iridium, thick $\mathbf{BL_1}$ anodes can be generated for only a few cents per square centimeter.[56] Thin layers (invisible to the naked eye on Au or Pt) of $\mathbf{BL_1}$ with approximately 35 nmol cm^{-2} of iridium have comparable overpotentials (ca. 240 mV versus ca. 200 mV for the thick layers). However, their cost in iridium is only US $5 per square meter, or 45 cents per square foot. As in the case of $\mathbf{BL_2}$, we find that only slightly thicker layers (still on the order of nmol cm^{-2}) of $\mathbf{BL_1}$ are required to reach maximum performance equivalent to the 2-μm thick layers (See Supporting Information, Figure S21).

Electrochemical generation of Ir_2O_3 from an iridium metal surface is another route to amorphous material, but requires an iridium(0) surface.[24] These preparations can be highly inefficient in terms of their use of iridium, or require exotic methods to prepare thin layers of the metal. Furthermore, the kinetics of the conversion of the metal to the oxide are significantly slower than the electrodeposition techniques we have developed for $\mathbf{BL_1}$ and $\mathbf{BL_2}$, as is evident by the long times required for generation of a significant amount of the redox-active layer from an iridium wire observable by voltammetry.[24]

The small hydroxide-capped iridium oxide nanoparticles **4** recently described in detail by Murray et al. are another attractive material for WO, as they display remarkably high turnover frequencies.[20] Looking at this material by EQCN reveals an unexpected instability in the electroflocculated layers of nanoparticles, however. At sufficiently reducing voltages (below the onset potential for catalysis) the nanoparticles clearly desorb from the surface of the anode. This is an unfortunate drawback, as a catalyst film left in a period of disuse and consequent depolarization will likely be unstable. Murray et al. have recently shown, though, that these small nanoparticles can be soluble, freely diffusing catalysts for water-oxidizing chemistry, rather than being surface-bound.[57] This opens up interesting opportunities for fundamental work in nanoparticle catalysis, in which piezoelectric gravimetry studies will no doubt play a role in disambiguating surface-bound from the solution-phase contributions to catalysis. Elucidating the phase of catalysis when working with soluble iridium materials is an important goal, especially during catalysis at long times.[58]

Furthermore, the subtle nature of the electrochemistry of iridium oxide is clarified by this work. As shown above in Figure 13, crystalline iridium dioxide has no electrochemical response below the threshold potential for the onset of WO. Consequently, unless great care is taken, one could be completely unaware of the presence of a thin layer of iridium dioxide on the electrode surface. With metallic conductivity, the layer is electrochemically silent until oxygen is evolved. Since the development of homogeneous catalysts for WO is ongoing, the presence of even minute amounts of iridium dioxide or related materials can clearly be a complicating and difficult-to-detect impurity in typical catalyst screening methods such as CV.

Each of the heterogeneous catalysts $\mathbf{BL_1}$, $\mathbf{BL_2}$, and the layer generated from **3** show unique voltammetry and deposition kinetics. Thus, we conclude that the nature of the material on the electrode surface is different in each case. One key contribution to these differences is the range of deposition kinetics measured by EQCN for the various materials. The

dx.doi.org/10.1021/ic300764f | Inorg. Chem. 2012, 51, 7749−7763

change in redox properties could arise, in part, because of kinetic effects that contribute to the formation of defect sites.[43] In all cases, it is likely that the oxidized form of the materials are conductive; there is no loss of electrochemical response upon formation of thick layers as measured by voltammetry and EQCN, and there is quick oxidation of the reduced (yellow-green) forms of $\mathbf{BL_1}$ and $\mathbf{BL_2}$ to form the blue form, as shown in the spectroelectrochemical data. However, the complete reduction of the surface layers is slower, suggesting that the reduced forms of $\mathbf{BL_1}$ and $\mathbf{BL_2}$ are semiconducting or perhaps insulating. In the case of the layer generated from **3**, the increase in capacitance over the entire voltammetric cycling range could be indicative of increasing electrode surface area, or a manifold of unresolved redox events. Along this line, it may be that the Cp* or Cp ligands in **1** and **2**, respectively, template the formation of surface material(s) dominated by the iridium center(s) which are responsible for the electrochromic behavior. Alternatively, the carbon content of $\mathbf{BL_1}$ and $\mathbf{BL_2}$ could contribute to these differences (e.g., by a carboxylic-acid oxidation product functioning as an O-donor ligand to iridium), but this proposal is beyond the scope of this report and will be dealt with in a future publication.

Once deposited, the amorphous films function as catalysts with essentially identical overpotentials and H/D isotope effects. To make this comparison though, we relied on our new EQCN method to deposit very thin layers of amorphous iridium material at similar loadings. This suggests that the catalytically active sites in the thin films are comparable despite the other differences. Complexes **1** and **2** offer unique benefits as precursor materials, however, as powders or the solutions of precursor are stable essentially indefinitely and give robustly adherent materials by simple voltammetry. Thicker preparations of catalyst can also be prepared with the organometallics **1** and **2**, in contrast to precursor **3** that does not form thick layers. These thick preparations of $\mathbf{BL_1}$ and $\mathbf{BL_2}$ exhibit morphology differences that have an effect on the catalytic activity of the anode. In our simple comparison with a thick film, we found that $\mathbf{BL_1}$ was more active than $\mathbf{BL_2}$ by around 15%. Thus, the identity of the ligand(s) on the soluble precursors has an effect on the deposited material. This opens a route to heterogeneous WO catalysts that may be tuned with molecular precursor chemistry. Optimization of heterogeneous catalysts in this way may provide materials suitable for the wide ranging conditions proposed as part of various schemes for artificial photosynthesis.[59]

CONCLUSIONS

Using an EQCN and a suite of other electrochemical techniques, we have compared the formation and activity of heterogeneous amorphous iridium WO catalysts. Deposition of layers from organometallic precursors **1** and **2**, which bear the pentamethylcyclopentadienyl or cyclopentadienyl ligands, respectively, gives rise to robustly adherent electrochromic layers of an iridium oxide that most closely resemble hydrous Ir_2O_3. The deposition rates of complexes **1** and **2** are distinct in each case, and related deposition behavior has not been observed with other half-sandwich iridium complexes bearing bidentate chelate ligands surveyed by electrochemistry. Solutions of **1** and **2** are stable during deposition and can be used to generate multiple films, which compares favorably with iridium hydroxide **3** and small hydroxide-capped iridium oxide nanoparticles **4**, the more traditional precursors to iridium oxide materials. EQCN reveals differences in the deposition kinetics and stability of the iridium oxide materials arising from each of the precursors; specifically, the small nanoparticles may be considered more useful as diffusional nanoparticle catalysts, as they are not stably adherent to the anode at less-oxidizing potentials. Taken together, our results show that amorphous iridium oxides are a promising class of materials for water-oxidizing chemistry, and further developments should be possible by judicious choice of precursor complexes.

EXPERIMENTAL SECTION

General Procedures. ^{1}H NMR spectra were collected on a 400 MHz Bruker spectrometer and referenced to the residual protio-solvent signal. $^{13}C\{^1H\}$ NMR spectra were collected on a 500 MHz Varian spectrometer and referenced to the solvent ^{13}C signal. ^{1}H and $^{13}C\{^1H\}$ NMR spectra of **2** in D_2O, 1 M D_2SO_4, and saturated Na_2SO_4 in D_2O can be found in the Supporting Information and were referenced to an internal standard using a solution of sodium 3-(trimethylsilyl)tetradeuteriopropionate in D_2O in a sealed capillary placed in the NMR tube. δ is reported in units of ppm and J in Hz. Elemental analyses were performed by Atlantic Microlab, Inc. $[(\eta^5\text{-}C_5Me_5)Ir(H_2O)_3]SO_4$[60] (**1**) and $[CpIrI_2]_x$[33] were obtained according to published procedures.

$(\eta^5\text{-}C_5H_5)IrSO_4\cdot nH_2O$ (2). $[(\eta^5\text{-}C_5H_5)IrI_2]_x$ (0.0730 g, 0.143 mmol), silver sulfate (0.0450 g, 0.144 mmol), and 3 mL of degassed deionized water were combined in a Schlenk flask under N_2 with exclusion of light and stirred 16 h. The crude reaction was then filtered through a glass fiber pad under air and evaporated to dryness. Yield 0.0547 g (98%). ^{1}H NMR (500 MHz, DMSO-d_6) δ 6.45 (s). ^{13}C NMR (126 MHz, DMSO-d_6) δ 86.60. Anal. Calcd for $Ir_1S_1O_4C_5H_5\cdot 2H_2O$. C, 15.42; H, 2.33; Found: C, 15.16; H, 2.14. Crystal samples of **2** used for X-ray crystallography were obtained by slow evaporation of a concentrated aqueous solution in an unstoppered vial.

CV. The measurements were made on a Princeton Applied Research Versastat 4-400 or model 273 potentiostat/galvanostat using a standard three-electrode configuration. A basal-plane graphite electrode (surface area: 0.09 cm^2) was used as the working electrode to minimize background oxidation current. The preparation and treatment of the basal-plane graphite electrode has been described previously.[33] A platinum wire was used as the counter electrode, and a Ag/AgCl electrode (Bioanalytical Systems, Inc.) was used as the reference (Ag/AgCl vs NHE: +197 mV). Experiments were generally carried out in unbuffered solutions containing 0.1 M KNO_3 (Strem Chemicals) as the supporting electrolyte. The solution pH was adjusted with dilute potassium hydroxide or nitric acid in some experiments, as noted.

EQCN. Simultaneous CV and piezoelectric gravimetry measurements were collected with an Elchema EQCN-600 nanobalance and an Elchema PS-605B potentiostat. Both instruments were computer-controlled with the Elchema Voltscan program (version V.4.1). A conventional three-electrode cell configuration was used; the counter electrode was a platinum foil, and an Ag/AgCl electrode (Bioanalytical Systems, Inc.) served as the reference. The working electrode was a 14-mm diameter quartz crystal (AT cut, plano−plano, 10 MHz) coated with a gold/chromium conducting surface (approximate electroactive surface area: 0.256 cm^2). The quartz crystal disk was mounted in an EQCM-5710 quartz crystal holder (Institute of Physical Chemistry, Polish Academy of Sciences, Warsaw, Poland). The frequency response of the quartz crystal was additionally monitored before and during experiments using a Fluke PM6680B high-resolution frequency counter.

Scanning Electron Microscopy. SEM images were obtained with an FEI ESEM XL-30 system. After film preparation on FTO-coated glass (Hartford Glass Co., Hartford City, Indiana), samples were rinsed, allowed to dry at room temperature, and then imaged within one day. Images and data were collected with an acceleration voltage of 10 keV.

dx.doi.org/10.1021/ic300764f | Inorg. Chem. 2012, 51, 7749−7763

Spectroelectrochemistry. For the spectroelectrochemistry experiments, a 1-cm path length quartz cuvette was used, with a narrow piece of FTO-coated glass as a working electrode (dimensions: 5 cm × 0.85 cm). The cuvette also contained the Pt-wire counter electrode and Ag/AgCl reference, outside the beam path of the spectrometer. UV−visible spectra were collected using a Varian Cary 50 Bio UV−visible spectrometer.

Clark-Electrode Oxygen Detection. Real-time measurements of oxygen evolution coupled to electrochemical oxidation were made with a YSI Clark-type oxygen electrode. Prior to beginning each set of experiments, the oxygen-permeable membrane was replaced to ensure a high-quality response and complete electrical isolation of the Clark electrode from the bulk solution. The electrodes were inserted into a tight-fitting water-jacketed glass vessel with the appropriate connections for the gold working (surface area: 0.017 cm^2) and Ag/AgCl reference electrodes, and a second chamber for the platinum counter electrode. The Clark electrode was immersed in the solution with the working and reference electrodes, allowing the real-time measurement of dissolved oxygen generated at the working electrode. The system was kept at a constant temperature of 25 °C. In a typical experiment, a freshly prepared electrolyte solution in Milli-Q water (7.5 mL, 0.1 M KNO_3) was allowed to equilibrate over minutes before electrolysis was initiated. The working electrode (without catalyst) was polarized to 1.4 V vs NHE for approximately 10 min in the electrolyte to collect the background current and oxygen production, after which time the electrode was switched off, the electrode prepared with catalyst, and the oxygen detection experiment rerun with the catalyst present. Basal-plane graphite electrodes are unsuitable for this experiment, as they undergo extensive oxidative damage over the timecourse required.

Rotating-Disk Electrode (RDE) Electrochemistry. RDE studies were carried out in a single-chamber cell configuration with a Princeton Applied Research Model 616 variable-speed rotator. The reference was an Ag/AgCl electrode (Bioanalytical Systems, Inc.) and the counter electrode was a platinum wire. The disk (surface area: 0.196 cm^2) material was platinum (Pine E3). In the case of the experiment where the platinum disk with catalyst required annealing, a Pine E6-series ChangeDisk RRDE assembly was used with a Pine MSR variable-speed rotator. The ring electrode (platinum) was not used in the experiment.

Kinetic Isotope Effect Measurement. The H/D KIE measurements were made using thin layers of catalyst prepared with potential cycling, analogous to those used for the Tafel plot. After deposition of the catalyst layer onto the platinum RDE, the RDE was rinsed with copious amounts of H_2O or D_2O, and then transferred to a solution of O_2-saturated H_2O or 99.9% D_2O (Cambridge Isotope Laboratories, Cambridge, MA) with 0.1 M KNO_3. The H/D KIE was then measured as the ratio of the steady-state current density at 1.2 V vs NHE in H_2O versus D_2O. No attempt was made to correct for the differences in pH vs pD. The measured pH value of both solutions was pH 6.

■ ASSOCIATED CONTENT

Ⓢ Supporting Information

NMR spectra for **2**. X-ray crystallographic details for **2**, and $CpIrSO_4(S\text{-}DMSO)_2{\cdot}H_2O$. Additional electrochemistry data. This material is available free of charge via the Internet at http://pubs.acs.org.

■ AUTHOR INFORMATION

Corresponding Author

*E-mail: gary.brudvig@yale.edu (G.W.B.), robert.crabtree@yale.edu (R.H.C.), francis.dsouza@unt.edu (F.D.).

Present Address

[‖]Beckman Institute and Division of Chemistry and Chemical Engineering, California Institute of Technology, MC 139-74, Pasadena, California 91106, United States.

Notes

The authors declare no competing financial interest.

■ ACKNOWLEDGMENTS

This work was supported as part of the Argonne-Northwestern Solar Energy Research (ANSER) Center, an Energy Frontier Research Center funded by the U.S. Department of Energy, Office of Science, Office of Basic Energy Sciences under Award DE-SC0001059 (G.W.B., R.H.C., and J.D.B.; the electrochemical experiments, isotope effect measurements, and EQCN experiments). Further funding from the Division of Chemical Sciences, Geosciences, and Biosciences, Office of Basic Energy Sciences of the U.S. Department of Energy through Grant DE-FG02-84ER13297 (R.H.C. and N.D.S.; synthesis and characterization of complexes; X-ray studies) and the U.S. National Science Foundation (CHE-1110942; EQCN studies) is gratefully acknowledged. The authors thank Ulrich Hintermair for helpful discussions.

■ REFERENCES

(1) (a) J. O'M. Bockris *Energy: The Solar Hydrogen Alternative*; Hogbin and Poole: Sydney, Australia, 1975. (b) Calvin, M. *Photochem. Photobiol.* **1976**, *23*, 425−44. (c) Porter, G.; Archer, M. D. *Interdiscip. Sci. Rev.* **1976**, *1*, 119−43. (d) Lehn, J. M.; Sauvage, J. P. *Nouv. J. Chim.* **1977**, *1*, 449−51. (e) Harriman, A. *J. Photochem.* **1984**, *25*, 33−6. (f) Harriman, A. *Platinum Met. Rev.* **1983**, *27*, 102−7. (g) Koryakin, B. V.; Dzhabiev, T. S.; Shilov, A. E. *Dokl. Akad. Nauk SSSR* **1977**, *233*, 620−2.

(2) (a) Limburg, J.; Vrettos, J. S.; Liable-Sands, L. M.; Rheingold, A. L.; Crabtree, R. H.; Brudvig, G. W. *Science* **1999**, *283*, 1524−1527. (b) Chen, H.; Tagore, R.; Olack, G.; Vrettos, J. S.; Weng, T.-C.; Penner-Hahn, J.; Crabtree, R. H.; Brudvig, G. W. *Inorg. Chem.* **2006**, *46*, 34−43. (c) Tagore, R.; Crabtree, R. H.; Brudvig, G. W. *Inorg. Chem.* **2008**, *47*, 1815−1823. (d) Cady, C. W.; Crabtree, R. H.; Brudvig, G. W. *Coord. Chem. Rev.* **2008**, *252*, 444−455.

(3) (a) Concepcion, J. J.; Jurss, J. W.; Templeton, J. L.; Meyer, T. J. *J. Am. Chem. Soc.* **2008**, *130*, 16462−16463. (b) Concepcion, J. J.; Jurss, J. W.; Brennaman, M. K.; Hoertz, P. G.; Patrocinio, A. O. T.; Iha, N. Y. M.; Templeton, J. L.; Meyer, T. J. *Acc. Chem. Res.* **2009**, *42*, 1954−1965. (c) Gilbert, J. A.; Eggleston, D. S.; Murphy, W. R., Jr.; Geselowitz, D. A.; Gersten, S. W.; Hodgson, D. J.; Meyer, T. J. *J. Am. Chem. Soc.* **1985**, *107*, 3855−3864. (d) Gersten, S. W.; Samuels, G. J.; Meyer, T. J. *J. Am. Chem. Soc.* **1982**, *104*, 4029−4030. (e) Moyer, B. A.; Meyer, T. J. *Inorg. Chem.* **1981**, *20*, 436−444. (f) Zong, R.; Thummel, R. P. *J. Am. Chem. Soc.* **2005**, *127*, 12802−12803. (g) Polyansky, D. E.; Muckerman, J. T.; Rochford, J.; Zong, R.; Thummel, R. P.; Fujita, E. *J. Am. Chem. Soc.* **2011**, *133*, 14649−14665. (h) Yamada, H.; Siems, W. F.; Koike, T.; Hurst, J. K. *J. Am. Chem. Soc.* **2004**, *126*, 9786−9795. (i) Cape, J. L.; Lymar, S. V.; Lightbody, T.; Hurst, J. K. *Inorg. Chem.* **2009**, *48*, 4400−4410.

(4) (a) Wasylenko, D. J.; Ganesamoorthy, C.; Borau-Garcia, J.; Berlinguette, C. P. *Chem. Commun.* **2011**, *47*, 4249−4251. (b) Yin, Q.; Tan, J. M.; Besson, C.; Geletii, Y. V.; Musaev, D. G.; Kuznetsov, A. E.; Luo, Z.; Hardcastle, K. I.; Hill, C. L. *Science* **2010**, *328*, 342−345. (c) Stracke, J. J.; Finke, R. G. *J. Am. Chem. Soc.* **2011**, *133*, 14872−14875.

(5) McDaniel, N. D.; Coughlin, F. J.; Tinker, L. L.; Bernhard, S. *J. Am. Chem. Soc.* **2007**, *130*, 210−217.

(6) (a) Harriman, A.; Pickering, I. J.; Thomas, J. M.; Christensen, P. A. *J. Chem. Soc., Faraday Trans. 1* **1988**, *84*, 2795−2806. (b) Harriman, A.; Thomas, J. M.; Millward, G. R. *New J. Chem.* **1987**, *11*, 757−62.

(7) Kiwi, J.; Graetzel, M. *Angew. Chem.* **1978**, *90*, 900−901.

(8) (a) Brunschwig, B. S.; Chou, M. H.; Creutz, C.; Ghosh, P.; Sutin, N. *J. Am. Chem. Soc.* **1983**, *105*, 4832−4833. (b) El Wakkad, S. E. S.; Hickling, A. *Trans. Faraday Soc.* **1950**, *46*, 820−824. (c) Kanan, M. W.; Nocera, D. G. *Science* **2008**, *321*, 1072−1075. (d) McAlpin, J. G.; Surendranath, Y.; Dinca, M.; Stich, T. A.; Stoian, S. A.; Casey, W. H.; Nocera, D. G.; Britt, R. D. *J. Am. Chem. Soc.* **2010**, *132*, 6882−6883. (e) Risch, M.; Klingan, K.; Ringleb, F.; Chernev, P.; Zaharieva, I.; Fischer, A.; Dau, H. *ChemSusChem* **2012**, *5*, 542−549.

(9) Mills, A.; Russell, T. *J. Chem. Soc., Faraday Trans.* **1991**, *87*, 1245−1250.
(10) (a) Smith, W. *J. Power Sources* **2000**, *86*, 74−83. (b) Millet, P.; Andolfatto, F.; Durand, R. *Int. J. Hydrogen Energy* **1996**, *21*, 87−93.
(11) Pourbaix, M. *Atlas of Electrochemical Equilibria in Aqueous Solutions*; Pergamon Press: Elmsford, NY, 1966.
(12) Greenwood, N. N.; Earnshaw, A. *Chemistry of the Elements*, 2nd ed.; Elsevier: Oxford, U.K., 1997.
(13) Gottesfeld, S.; Srinivasan, S. *J. Electroanal. Chem. Interfacial Electrochem.* **1978**, *86*, 89−104.
(14) Lufaso, M. W.; Zur Loye, H.-C. *Inorg. Chem.* **2005**, *44*, 9143−9153.
(15) (a) Yamanaka, K. *Jpn. J. Appl. Phys., Part 1* **1989**, *28*, 632−637. (b) Baur, J. E.; Spaine, T. W. *J. Electroanal. Chem.* **1998**, *443*, 208−216.
(16) Nahor, G. S.; Hapiot, P.; Neta, P.; Harriman, A. *J. Phys. Chem.* **1991**, *95*, 616−621.
(17) Petit, M. A.; Plichon, V. *J. Electroanal. Chem.* **1998**, *444*, 247−252.
(18) Zhao, Y.; Hernandez-Pagan, E. A.; Vargas-Barbosa, N. M.; Dysart, J. L.; Mallouk, T. E. *J. Phys. Chem. Lett.* **2011**, *2*, 402−406.
(19) Zhao, Y.; Vargas-Barbosa, N. M.; Hernandez-Pagan, E. A.; Mallouk, T. E. *Small* **2011**, *7*, 2087−2093.
(20) Nakagawa, T.; Beasley, C. A.; Murray, R. W. *J. Phys. Chem. C* **2009**, *113*, 12958−12961.
(21) Bestaoui, N.; Prouzet, E. *Chem. Mater.* **1997**, *9*, 1036−1041.
(22) (a) Profeti, D.; Lassali, T. A. F.; Olivi, P. *J. Appl. Electrochem.* **2006**, *36*, 883−888. (b) Sardar, K.; Fisher, J.; Thompsett, D.; Lees, M. R.; Clarkson, G. J.; Sloan, J.; Kashtiban, R. J.; Walton, R. I. *Chem. Sci.* **2011**, *2*, 1573−1578. (c) Mugavero, S. J., III; Smith, M. D.; Yoon, W.-S.; zur Loye, H.-C. *Angew. Chem., Int. Ed.* **2009**, *48*, 215−218.
(23) Trasatti, S. *Electrochim. Acta* **1984**, *29*, 1503−1512.
(24) (a) Stonehart, P.; Kozlowska, H. A.; Conway, B. E. *Proc. R. Soc. London A* **1969**, *310*, 541−563. (b) Rand, D. A. J.; Woods, R. *J. Electroanal. Chem. Interfacial Electrochem.* **1974**, *55*, 375−381. (c) Capon, A.; Parsons, R. *J. Electroanal. Chem. Interfacial Electrochem.* **1972**, *39*, 275−286. (d) Buckley, D. N.; Burke, L. D. *J. Chem. Soc., Faraday Trans. 1* **1975**, *71*, 1447−1459. (e) Pickup, P. G.; Birss, V. I. *J. Electroanal. Chem. Interfacial Electrochem.* **1987**, *220*, 83−100.
(25) Hunt, L. B. *Platinum Met. Rev.* **1987**, *31*, 32−41.
(26) (a) MacNamara, E. L. *J. Electrochem. Soc.* **1962**, *109*, 61−63. (b) El Sawy, E. N.; Birss, V. I. *J. Mater. Chem.* **2009**, *19*, 8244−8252.
(27) (a) Beni, G.; Schiavone, L. M.; Shay, J. L.; Dautremont-Smith, W. C.; Schneider, B. S. *Nature* **1979**, *282*, 281−283. (b) Khakani, M. A.; Chaker, M.; Gat, E. *Appl. Phys. Lett.* **1996**, *69*, 2027−2029.
(28) Gottesfeld, S.; McIntyre, J. D. E.; Beni, G.; Shay, J. L. *Appl. Phys. Lett.* **1978**, *33*, 208−210.
(29) Conway, B. E.; Mozota, J. *Electrochim. Acta* **1983**, *28*, 9−16.
(30) Burke, L. D.; Whelan, D. P. *J. Electroanal. Chem. Interfacial Electrochem.* **1981**, *124*, 333−337.
(31) Galsboel, F.; Larsen, S.; Rasmussen, B.; Springborg, J. *Inorg. Chem.* **1986**, *25*, 290−297.
(32) Hull, J. F.; Balcells, D.; Blakemore, J. D.; Incarvito, C. D.; Eisenstein, O.; Brudvig, G. W.; Crabtree, R. H. *J. Am. Chem. Soc.* **2009**, *131*, 8730−8731.
(33) Blakemore, J. D.; Schley, N. D.; Balcells, D.; Hull, J. F.; Olack, G. W.; Incarvito, C. D.; Eisenstein, O.; Brudvig, G. W.; Crabtree, R. H. *J. Am. Chem. Soc.* **2010**, *132*, 16017−16029.
(34) Schley, N. D.; Blakemore, J. D.; Subbaiyan, N. K.; Incarvito, C. D.; D'Souza, F.; Crabtree, R. H.; Brudvig, G. W. *J. Am. Chem. Soc.* **2011**, *133*, 10473−10481.
(35) Blakemore, J. D.; Schley, N. D.; Olack, G. W.; Incarvito, C. D.; Brudvig, G. W.; Crabtree, R. H. *Chem. Sci.* **2011**, *2*, 94−98.
(36) This carbon admixture, which is not completely lost even after hours of electrolysis, will be described in detail in a future report.
(37) Fine, D. A. *Inorg. Chem.* **1969**, *8*, 1014−1016.
(38) (a) Beutler, P.; Gamsjager, H. *J. Chem. Soc., Chem. Commun.* **1976**, 554−555. (b) Gamsjager, H.; Beutler, P. *J. Chem. Soc., Dalton Trans.* **1979**, 1415−1418. (c) Castillo-Blum, S. E.; Richens, D. T.; Sykes, A. G. *Inorg. Chem.* **1989**, *28*, 954−960.
(39) Hintermair, U.; Hashmi, S. M.; Elimelech, M.; Crabtree, R. H. *J. Am. Chem. Soc.* **2012**, *134* (23), 9785−9795.
(40) Wöhler, L.; Witzmann, W. *Z. Anorg. Chem.* **1908**, *57*, 323−352.
(41) Buttry, D. A.; Ward, M. D. *Chem. Rev.* **1992**, *92*, 1355−79.
(42) Longer EQCN experiments are complicated by the fact that the solutions are not stirred. Under the conditions, we did not observe any unexpected changes in the mass readout over the time course of the 20 min experiments here. Additionally, there was no indication that the voltammetry was limited by depletion of the bulk concentration near the electrode.
(43) Zaharieva, I.; Chernev, P.; Risch, M.; Klingan, K.; Kohlhoff, M.; Fischer, A.; Dau, H. *Energy Environ. Sci.* **2012**, *5*, 7081−7089.
(44) Burke, L. D.; Naser, N. S.; Ahern, B. M. *J. Solid State Electrochem.* **2006**, *11*, 655−666.
(45) By judicious choice of the cell geometry and volume, we can detect oxygen generated electrochemically at our working electrode surface with accuracy down to approximately ±5 nmol. (See Experimental Section for more details.)
(46) As reported before, thick layers deposited over longer times contain carbon in a lower proportion than is present in the precursor complex.[35] The carbon content of thin layers may be higher.
(47) Cracking also appears upon long-term storage at room temperature, presumably because of a similar dehydration process.
(48) (a) Hackwood, S.; Beni, G.; Gallagher, P. K. *Solid State Ionics* **1981**, *2*, 297−299. (b) Aurian-Blajeni, B.; Boucher, M. M.; Kimball, A. G.; Robblee, L. S. *J. Mater. Res.* **1989**, *4*, 440−446.
(49) Glarum, S. H.; Marshall, J. H. *J. Electrochem. Soc.* **1980**, *127*, 1467−1474.
(50) Gottesfeld, S.; McIntyre, J. D. E. *J. Electrochem. Soc.* **1979**, *126*, 742−750.
(51) Frame, F. A.; Townsend, T. K.; Chamousis, R. L.; Sabio, E. M.; Dittrich, T.; Browning, N. D.; Osterloh, F. E. *J. Am. Chem. Soc.* **2011**, *133*, 7264−7267.
(52) Yamada, H.; Siems, W. F.; Koike, T.; Hurst, J. K. *J. Am. Chem. Soc.* **2004**, *126*, 9786−9795.
(53) Limburg, J.; Vrettos, J. S.; Chen, H.; de Paula, J. C.; Crabtree, R. H.; Brudvig, G. W. *J. Am. Chem. Soc.* **2000**, *123*, 423−430.
(54) Morris, N. D.; Suzuki, M.; Mallouk, T. E. *J. Phys. Chem. A* **2004**, *108*, 9115−9119.
(55) Sivasankar, N.; Weare, W. W.; Frei, H. *J. Am. Chem. Soc.* **2011**, *133*, 12976−12979.
(56) A simple calculation of 16 mg of **1** per 40 cm^2 gives approximately 1 cent per cm^2 using \$14,000 mol^{-1} iridium (the price of $IrCl_3$ on an iridium basis from a major supplier). This calculation neglects the organic ligand, solvent, FTO glass and silver sulfate used in the preparation of **1**.
(57) Nakagawa, T.; Bjorge, N. S.; Murray, R. W. *J. Am. Chem. Soc.* **2009**, *131*, 15578−15579.
(58) Gambardella, A. A.; Bjorge, N. S.; Alspaugh, V. K.; Murray, R. W. *J. Phys. Chem. C* **2011**, *115*, 21659−21665.
(59) (a) Song, W.; Chen, Z.; Brennaman, M. K.; Concepcion, J. J.; Patrocinio, A. O. T.; Iha, N. Y. M.; Meyer, T. J. *Pure Appl. Chem.* **2011**, *83*, 749−768. (b) Wasielewski, M. R. *Acc. Chem. Res.* **2009**, *42*, 1910−1921. (c) Bard, A. J. *Ber. Bunsen-Ges. Phys. Chem.* **1988**, *92*, 1187−1194. (d) Khaselev, O.; Turner, J. A. *Science* **1998**, *280*, 425−427. (e) Kocha, S. S.; Montgomery, D.; Peterson, M. W.; Turner, J. A. *Sol. Energy Mater. Sol. Cells* **1998**, *52*, 389−397. (f) McKone, J. R.; Warren, E. L.; Bierman, M. J.; Boettcher, S. W.; Brunschwig, B. S.; Lewis, N. S.; Gray, H. B. *Energy Environ. Sci.* **2011**, *4*, 3573−3583. (g) Gray, H. B. *Nat. Chem.* **2009**, *1*, 7.
(60) Ogo, S.; Makihara, N.; Watanabe, Y. *Organometallics* **1999**, *18*, 5470−5474.